Chemical properties, sources and size-resolved hygroscopicity of submicron black carbon-containing aerosols in urban Shanghai

Shijie Cui[1], Dan Dan Huang[2], Yangzhou Wu[1,a], Junfeng Wang[1], Fuzhen Shen[1,b], Jiukun Xian[1], Yunjiang Zhang[1], Hongli Wang[2], Cheng Huang[2], Hong Liao[1], Xinlei Ge[1,*]

[1] Jiangsu Key Laboratory of Atmospheric Environment Monitoring and Pollution Control, Collaborative Innovation Center of Atmospheric Environment and Equipment Technology, School of Environmental Science and Engineering, Nanjing University of Information Science and Technology, Nanjing 210044, China

[2] Shanghai Academy of Environmental Sciences, Shanghai 200233, China

[a]now at: Department of Atmospheric Sciences, School of Earth Sciences, Zhejiang University, Hangzhou 310027, PR China

[b]now at: Department of Meteorology, University of Reading, Reading, RG6 6BX, UK

*Corresponding author: Xinlei Ge (Email: caxinra@163.com)

For *Atmospheric Chemistry and Physics*

Abstract. Refractory black carbon (rBC) aerosols play an important role in air quality and climate change, yet high time-resolved and detailed investigation on the physicochemical properties of rBC and its associated coating is still scarce. In this work, we used a laser-only Aerodyne soot particle aerosol mass spectrometer (SP-AMS) to exclusively measure the rBC-containing (rBCc) particles, and compared their properties with the total non-refractory submicron particles (NR-PM$_1$) measured in parallel by a high-resolution AMS (HR-AMS) in Shanghai. The observation shows that rBC was overall thickly coated with an average mass ratio of coating to rBC core (R_{BC}) of ~5.0 (±1.7). However, mass of rBC coating species only occupied 19.1 (± 4.9)% of those in NR-PM$_1$; sulfate tended to condense preferentially on non-rBC particles therefore its portion on rBC was only 7.4 (± 2.2)%, while the majority of primary organic aerosols (POA) were associated with rBC (72.7 ± 21.0%). Positive matrix factorization reveals that cooking emitted organics did not coat on rBC, and a portion of organics coated on rBC was from biomass burning which was unidentifiable in NR-PM$_1$. Small rBCc particles were predominantly from traffic, while large-sized ones were often mixed with secondary components and typically had thick coating. Sulfate and secondary organic aerosol (SOA) species were generated mainly through daytime photochemical oxidation (SOA formation likely involved with in-situ chemical conversion of traffic-related POA to SOA), while nocturnal heterogeneous formation was dominant for nitrate; we also estimated the average times of 5~19 hours for those secondary species to coat on rBC. Particles during a short period that was affected by ship emissions, were characterized with a high vanadium concentration (on average 6.3 ± 3.1 ng m^{-3}) and a mean vanadium/nickel mass ratio of 2.0 (± 0.6). Furthermore, the size-resolved hygroscopicity parameter (κ_{rBCc}) of rBCc particles was obtained based on its fully chemical characterization, and was parameterized as $\kappa_{rBCc}(x)= 0.29-0.14 \times \exp(-0.006 \times x)$ (x is from 150 to 1000 nm). Under critical supersaturations (SS_C) of 0.1% and 0.2%, the D_{50} values were 166 (± 16) and 110 (± 5) nm, respectively, and with 16 (± 3)% and 59 (± 4))% of rBCc in number could be activated into cloud condensation nuclei (CCN). Our findings are valuable to advance the understanding of BC chemistry as well as the effective control of atmospheric BC pollution.

1 Introduction

Refractory black carbon (rBC) aerosols can directly absorb solar radiation, indirectly change the nature of cloud and alter the albedo of snow or glaciers (Jacobi et al., 2015), resulting in a positive radiative forcing that is second only to carbon dioxide on both regional and global scales (Ramanathan and Carmichael, 2008;Bond et al., 2013). The fresh rBC particles produced by incomplete combustion of biomass and fossil fuel tend to be fractal in morphology and can mix with many other components (Peng et al., 2016;Li et al., 2021). After entering into the atmosphere, fresh rBC can further externally or internally mix with organic/inorganic species which are primarily emitted or secondarily formed, and such aged rBC-containing (rBCc) particles (Chen et al., 2017;Lee et al., 2017) might have contrasting chemical properties and morphologies (or mixing states) (Liu et al., 2017a;Lee et al., 2019;Xie et al., 2019). In addition, when rBC mixes with hydrophilic materials, its hygroscopicity, cloud condensation nuclei (CCN) activity and size distribution, etc., can be significantly changed, which subsquently affect its atmospheric behavior, impact and lifecycle (Liu et al., 2013;Lambe et al., 2015). Therefore, it is necessary to elucidate the physicochemical characteristics and sources of rBC cores and associated coating materials, so as to better understand their influences on climate and air quality.

Chemical composition of ambient rBCc particles is largely dependent upon atmospheric conditions and emission sources. In general, the thickness of coating, mass contribution of secondary components (such as sulfate, nitrate and secondary organic aerosol (SOA) species) and oxidation degree of the coated organics of rBCc particles, increase with the aging time or oxidation capacity of ambient environment (Cappa et al., 2012;Liu et al., 2015;Wang et al., 2017;Collier et al., 2018;Wang et al., 2019), except in some specific cases that thickly coated rBCc might be dominated by primarily emitted particles (such as from biomass burning (Wang et al., 2017)). Recent field observations report that SOA species coated on rBC cores could account for 35% and 41% of the total SOA mass near traffic emission sources and in a polluted offshore environment, respectively (Massoli et al., 2012;Massoli et al., 2015). A study of rBCc particles in Singapore finds that over 90% of rBC derived from local combustion

80   sources (mainly traffic), while 30% of rBC was associated with fresh SOA generated

81   under the influences of daytime shipping and industrial emissions (Rivellini et al.,

82   2020).The SOA material concentrated on the surface of rBC was found to be chemically

83   different from the SOA that was externally mixed with rBC (Lee et al., 2017) in Fontana,

84   California, and another study in Shenzhen, China, reveals that more oxidized SOA

85   preferred to mix with rBC due to that abundant transition metals detected on rBC cores

86   might act as catalysts to convert less oxidized SOA to more oxidized SOA in aerosol

87   aqueous phase (Cao et al., 2022); the rBC could catalyze SO_2 to form sulfate as well,

88   as observed in Beijing (Zhang et al., 2020) and Guangzhou (Zhang et al., 2021), China.

89   Besides SOA, cooking-related OA is found to be externally mixed with rBC (Lee et al.,

90   2017;Wang et al., 2019), and a unique biomass burning related OA factor was identified

91   and was only present in rBCc rather than non-rBC particles during summertime in

92   Beijing (Wang et al., 2020a).

93   Size distribution of rBCc particles is also modulated greatly by their original

94   sources and ageing processes. For example, a study in Shanghai shows a bimodal size

95   distribution of rBCc, with a condensation mode dominated by traffic emissions (small

96   core size, thin coating) and a droplet mode including highly aged biomass burning

97   particles (large core size and thick coating) and highly aged traffic particles (small core

98   size and very thick coating) (Gong et al., 2016). Another study in Beijing (Liu et al.,

99   2019) further resolves four size modes of rBCc, relevant with traffic (small core, thin

100 coating), coal or biomass burning (moderate coating, both small and large cores), coal

101 combustion (large core, think coating) and secondary process (thick coating, both small

102 and large cores).

103   Moreover, water uptake and CCN activity of rBCc particles can increase with the

104 encapsulation of water-soluble substances such as sulfate, nitrate, and SOA (Liu et al.,

105 2013;Wu et al., 2019). Based on the measured chemical composition of rBCc, our

106 previous work has established a method for calculating size-resolved hygroscopicity

107 parameters of rBCc ($\kappa_{r\text{BCc}}$), and determined the CCN activation diameters of rBC

108 particles for given critical supersaturation (SS_C) values (Wu et al., 2019).

109   Highly time-resolved chemical characterization of rBCc particles were seldom

110 reported in China and is still lacking in Shanghai. In this study, we utilized an Aerodyne

111 soot particle aerosol mass spectrometer (SP-AMS) to determine the concentration,

112 composition and size distribution of rBCc particles exclusively (technical details in

113 Section 2.1) in urban Shanghai for the first time. We also compared the SP-AMS

114 measurement results with those from a co-located Aerodyne high-resolution time-of-

115 flight aerosol mass spectrometer (HR-AMS), to comprehensively investigate the

116 characteristics of rBCc particles. We analyzed $\kappa_{r\text{BCc}}$ and estimated the proportions of

117 activated rBCc numbers at given SS_C as well.

118

119 **2 Experimental methods**

120 **2.1 Sampling site and instrumentation**

121 The field measurement was conducted from October 31 to December 2, 2018,

122 during which the instruments were deployed on 8th floor of the building of Shanghai

123 Academy of Environmental Sciences (SAES) (31°10'33.348" N, 121°26'10.978" E).

124 Shanghai can be a representative of the densely populated megacity across the world;

125 the measurement period also belonged to the cold season when sources of rBCc might

126 be complex, and can offer rich information about the rBCc; of course, future

127 measurements in other seasons are still essential to achieve a complete understanding

128 of rBCc. East of the sampling site is a large commercial shopping center, and the site

129 is surrounded by residential areas with two busy arterial roads directly to the east (~450

130 m) and south (~150 m), respectively (Figure S1 in the supporting information). In

131 addition, the adjacent areas are densely populated with roadside residents, office

132 workers, and market traders, as well as crowds in and out of the Caobao Road Metro

133 station (~100 m). The measurement period was dominated by northeasterly winds,

134 while many international freight companies located on northeastern side of the site, and

135 many freighters were reposing on the Huangpu River. Overall, the sampling site was

136 probably influenced by vehicular emissions, residential activities and the northeast

137 Cargo ship emission plumes, etc.

138 An Aerodyne SP-AMS and an HR-AMS were operated in parallel during the

139 campaign. The two AMSs shared a same sampling line with a PM$_{2.5}$ cyclone (Model

140   URG-2000-30EN) in front to remove coarse particles. Ambient air pulled through the

141   sampling line was dried using a diffusion dryer filled with silicon gel and was

142   subsequently drawn into both instruments. Due to the transmission efficiency of the

143   inlet lens, both AMSs measured mainly particles of 30-1200 nm (denoted as PM_1).

144   The working principle of SP-AMS has been described in detail previously (Onasch

145   et al., 2012). However, in this work, we used only the intracavity infrared laser

146   vaporizer to selectively measure rBCc particles (rBC cores and associated coating

147   materials), as rBC can absorb 1064 nm laser light. The thermal tungsten vaporizer had

148   to be physically detached otherwise non-rBC particles can still be detected as the

149   filament can heat the vaporizer to ~200 ^{o}C even if it was turned off. Before sampling,

150   the SP-AMS was tuned and calibrated following the steps described previously (Lee et

151   al., 2015;Willis et al., 2016;Wang et al., 2017). During sampling, due to relatively low

152   rBCc mass loadings, the SP-AMS was operated with two mass sensitive V modes (2.5

153   minutes per cycle), one with a particle time-of-flight (PToF) mode (30 s) and another

154   one (120 s) with a mass spectral mode with mass-to-charge (m/z) ratio up to 500.

155   Filtered air was also measured in the middle of campaign (for 60 min) to determine the

156   limits of detection (LOD, three times the standard deviation) of various aerosol species

157   and to adjust the air-influenced mass spectral signals (Zhang et al., 2005).

158   Before removal of the tungsten heater, the calibrations of ionization efficiency (IE)

159   for nitrate and relative ionization efficiency (RIE) of sulfate were performed by using

160   pure ammonium nitrate and ammonium sulfate particles (Jayne et al., 2000), and the

161   values were assumed to be unchanged throughout the whole campaign (Willis et al.,

162   2016). RIE of rBC to nitrate was calibrated by using size-selected (300 nm) BC

163   particles (REGAL 400R pigment black, Cabot Corp.) (Onasch et al., 2012), and the

164   average ratio of C_1^+ to C_3^+ was calculated to be 0.584 to correct the interference on C_1^+

165   from other organics. RIEs of ammonium, nitrate, sulfate and rBC were determined to

166   be 4.53, 1.10, 1.01, and 0.17, respectively, and RIE of organics used the default value

167   of 1.4 (Canagaratna et al., 2007). The size was calibrated by Polystyrene latex (PSL)

168   spheres (100–700 nm) (Duke Scientific Corp., Palo Alto, CA) before the measurement.

169   This study applied a collection efficiency (CE) of 0.5 for SP-AMS.

170   The co-located HR-AMS (DeCarlo et al., 2006) was used to measure all PM_1

171   including both rBCc and non-rBC particles, but it detected only non-refractory species

172   (NR-PM_1 species) as its 600 $^\circ$C thermal heater is unable to vaporize rBC and other

173   refractory components. In addition, mass concentrations of gaseous pollutants, carbon

174   monoxide (CO), ozone (O_3), nitrogen dioxide (NO_2), and sulfur dioxide (SO_2) were

175   measured by the Thermo Scientific analyzers provided by SAES. Meteorological

176   parameters including air temperature (T), relative humidity (RH), wind speed (WS),

177   wind direction (WD) and precipitation, were obtained from Xujiahui Environmental

178   Monitoring Station of Shanghai (31°11'49.1424"N, 121°26'34.44" E)(~2400 m away

179   from the site). The concentrations of particle-phase vanadium (V) and nickel (Ni) that

180   were used to investigate ship influence were measured independently by an

181   Atmospheric heavy metal analyzer (XHAM-2000A, SAIL HERO., China).

182

183   **2.2 Data analysis**

184   The AMS data (both SP-AMS and HR-AMS) were analyzed using standard ToF-

185   AMS data analysis tool (Squirrel version 1.59D and Pika version 1.19D), based on Igor

186   Pro 6.37 (Wavemetrics, Lake Oswego, OR, USA). The mass concentrations and high

187   resolution mass spectra (HRMS) of rBC and coating species (rBC$_{CT}$) were calculated

188   from high-resolution (HR) fitting of V-mode data. Size distributions of rBCc

189   components were determined by the PToF data with unit mass resolution and were

190   scaled to their mass concentrations obtained above. In particular, size distribution of

191   rBC was scaled to that of m/z 24 (C_2^+) (the scaling factor is rBC mass concentration to

192   that of calculated based on its size distribution), because m/z 24 as a rBC fragment, has

193   least interference from other organic or inorganic species; such treatment was adopted

194   in earlier studies too (Collier et al., 2018;Wang et al., 2019;Wang et al., 2016).

195   The HR ion fitting of AMS data is able to distinguish various ions and isotopic

196   ions and calculate elemental ratios of organics such as oxygen-to-carbon (O/C),

197   hydrogen-to-carbon (H/C), nitrogen-to-carbon (N/C), and organic mass to organic

198   carbon (OM/OC) ratios, via the original Aiken-ambient (A-A) method (Aiken et al.,

199   2008) and the improved method (I-A) (Canagaratna et al., 2015b). Outcomes of both

200 methods correlated well. Average O/C, H/C, and OM/OC ratios from the I-A method

201 used in this work were 24.9%, 7.3%, and 5.6%, respectively, higher than those from the

202 A-A method.

203   Furthermore, we performed Positive matrix factorization (PMF) (Paatero and

204 Tapper, 1994) analysis on the HRMS of organics measured by the SP-AMS via the PMF

205 Evaluation Tool (Ulbrich et al., 2009). The PMF solutions were thoroughly evaluated

206 following the protocols documented in Zhang et al. (2011). Finally, a 6-factor solution

207 was chosen as the optimal one. The final result included four primary OA (POA) factors,

208 namely hydrocarbon-like species enriched OA (HOA-rich), rBC-enriched OA (rBC-

209 rich), biomass burning OA (BBOA), water-soluble hydrocarbon-like species enriched

210 OA (WS-HOA), and two secondary OA (SOA) factors including a less oxidized

211 oxygenated OA (LO-OOA$_{r\text{BC}}$), and a more oxidized oxygenated OA (MO-OOA$_{r\text{BC}}$)

212 (Key diagnostic plots in Fig. S2). As a comparison, the mass spectra of 5-factor and 7-

213 factor solutions are illustrated in Fig. S3 (for the 5-factor solution, factor 3 is a mixed

214 factor of BBOA and WS-HOA, while for the 7-factor solution, MO-OOA clearly

215 splits into factor 5 and factor 2). The HR-AMS data were processed in a similar way,

216 and four factors of NR-PM$_1$ organics were resolved, including hydrocarbon-related OA

217 (HOA$_{\text{NR-PM1}}$), cooking OA (COA$_{\text{NR-PM1}}$), less oxidized oxygenated OA (LO-OOA$_{\text{NR-}}$

218 $_{\text{PM1}}$), and more oxidized oxygenated OA (MO-OOA$_{\text{NR-PM1}}$) (Mass spectra and time

219 series shown in Fig. S4).

220

221   **2.3 Calculation of size-resolved hygroscopicity of rBCc**

222   The hygroscopicity parameter κ is a single parameter representing the

223 hygroscopicity of particles, calculated based on essentially the chemical composition

224 (Petters and Kreidenweis, 2007). SP-AMS measured size-resolved chemical

225 compositions of rBCc can thus lead to size-resolved hygroscopicity of rBCc ($\kappa_{r\text{BCc}}$)

226 (Wu et al., 2019;Hu et al., 2021). This study applied a similar method proposed by Wu

227 et al. (2019) and the critical parameters involved in calculation are detailed in Table S1.

228 The procedures are briefly described here: (1) obtain the matrice of size-resolved mass

229 concentrations of each rBCc component from SP-AMS analysis; (2) convert the size-

230   resolved concentration matrice of inorganic ions (SO_4^{2-}, NO_3^- and NH_4^+) to

231   corresponding matrice of inorganic salts (NH_4NO_3, NH_4HSO_4, $(NH_4)_2SO_4$) using a

232   simplified solution of ion pairs (Gysel et al., 2007); (3) convert the size-resolved mass

233   matrice of all components (inorganic salts, OA and rBC) to those of size-resolved

234   volume fractions (Gysel et al., 2007;Chang et al., 2010;Wu et al., 2016); (4) combine

235   with previously reported hygroscopic parameters (Gysel et al., 2007;Chang et al.,

236   2010;Wu et al., 2016) to obtain the volumetric contributions of each component to the

237   hygroscopicity of rBCc; (5) use the Zdanovskii-Stokes-Robinson (ZSR) rule to derive

238   the size-resolved hygroscopicity of rBCc (κ_{rBCc}) (Topping et al., 2005b, a).

239

240   **3 Results and discussion**

241   **3.1 Overview of chemical characteristics of rBCc and NR-PM$_1$ particles**

242   Figure 1 presents the time series of meteorological parameters, concentrations of

243   gaseous pollutants (CO, NO_2, O_3, and SO_2), ship emission tracers (vanadium and

244   nickel), rBC and rBC$_{CT}$ species and their mass percentages to the total rBCc mass,

245   PMF-resolved OA factors and their corresponding fractional contributions. The

246   sampling period was featured by relatively moderate temperatures and very stagnant

247   conditions with average ($\pm 1\sigma$) temperature of 15.3 ($\pm$ 2.9) °C and wind speed (WS) of

248   0.16 ($\pm$ 0.29) m s^{-1}. The wind with speeds <0.5 m s^{-1} dominated most of the sampling

249   days and 42% of sampling time was with near-zero wind, therefore overall influence of

250   WS and WD on surface mass loadings of rBCc was insignificant. Yet one should keep

251   in mind that WD can affect rBCc sources, and WS in higher altitude might be stronger

252   therefore long-range transport of air pollutants was still possible. The average

253   concentrations of CO, NO_2, O_3, SO_2, V, and Ni were determined to be 0.60 ($\pm$ 0.26)

254   ppm, 29.20 ($\pm$ 17.07) ppt, 27.10 ($\pm$ 15.97) ppt, 1.27 ($\pm$ 0.72) ppt, 4.05 ($\pm$ 3.19) ng m^{-3},

255   and 3.06 ($\pm$ 2.45) ng m^{-3}, respectively.

256   The mass loadings of rBC and rBC$_{CT}$ ranged from 0.04 to 11.00 μg m^{-3} and 0.37

257   to 30.47 μg m^{-3} with campaign-mean values ($\pm$ 1σ) of 0.92 ($\pm$ 0.81) μg m^{-3} and 4.55 ($\pm$

258   4.40) μg m^{-3}. The coating materials accounted for 81.8 ($\pm$ 5.3)% of the total rBCc mass,

259   of which organics was the most abundant species (2.54 $\pm$ 2.52 μg m^{-3}, 46.6 $\pm$ 6.4%),

260   followed by nitrate (1.20 ± 1.30 µg m^{-3}, 18.5 ± 8.0%), ammonium (0.44 ± 0.40 µg m^{-3},

261   8.0 ± 2.0%), sulfate (0.30 ± 0.19 µg m^{-3}, 7.1 ± 3.6%), and chloride (0.07 ± 0.05 µg m^{-3},

262   1.7 ± 1.0%). The mass ratio of rBC$_{CT}$ to rBC (R_{BC}) ranged from 2.2 to 9.0, with an

263   average of ~5.0 (± 1.7). The average R_{BC} was higher than that in California ($R_{BC} = 2.3$)

264   (Collier et al., 2018) and in Shenzhen ($R_{BC} = 2.5$)(Cao et al., 2022), lower than that in

265   Tibetan Plateau ($R_{BC}=7.7$) (Wang et al., 2017) and similar to that in Beijing ($R_{BC}=5.0$)

266   (Wang et al., 2019), suggesting rBC was relatively thickly coated throughout the

267   campaign. Correlation between rBC and rBC$_{CT}$ was moderate (Pearson's $r = 0.76$).

268   Correlation coefficients (r) of chloride, nitrate, sulfate and organics with rBC were 0.72,

269   0.87, 0.71 and 0.73, respectively, suggesting variability of sources among different

270   coating components.

271   Figure 2 compares the campaign-averaged diurnal patterns of rBC$_C$ and NR-PM$_1$

272   species, chemical compositions of rBCc and NR-PM$_1$, and mass ratios of the species

273   coated on rBC to those of NR-PM$_1$. We found that the diurnal variations of nitrate,

274   sulfate, ammonium, chloride were very similar ($r > 0.92$) between the two particle

275   groups, while apparent difference was found for rBCc organics with a much obvious

276   morning rush hour peak (6:00 - 9:00). The results indicate that the formation processes

277   of inorganic salts coated on rBC were similar to those uncoated on rBC, but there were

278   large difference regarding sources/processes existed for organics. For rBC itself, the

279   diurnal cycle presented clearly a morning peak and an evening peak, likely relevant

280   with rush hour traffic emissions (CO showed similar pattern). On the contrary, R_{BC} had

281   a minimum in the morning and dropped to a low level in later afternoon, probably due

282   to influence from traffic-emitted fresh and barely coated rBC particles (details in

283   Section 3.2.1).

284   Distributions of species between rBCc and non-rBC particles were also different,

285   leading to different chemical compositions (Figs. 2g and 2h). Sulfate tended to

286   preferentially condense on non-rBC particles, as its mass contribution to total rBCc

287   mass was only 6.5 (± 4.2)%, while its contribution to total NR-PM$_1$ was 17.6 (± 8.3)%.

288   Apportionment of nitrate between rBCc and non-rBC particles was about even as it

289   both occupied ~26% of the total rBCc and NR-PM$_1$ masses. Organics occupied 55.9 ($\pm$

290 9.2)% of rBCc mass, larger than it in NR-PM$_1$ (43.7 ± 11.7%), due to that primary OA

291 species preferentially associated with rBC. Such result is similar to that observed in

292 winter in Beijing but contrary to the result that SOA was more abundant in rBCc in

293 Shenzhen (Cao et al., 2022).

294   On average, rBC$_C$ accounted for 19.1% of the total NR-PM$_1$ mass loading (21.61

295 ± 15.80 μg m^{-3})(Fig. 2i), comparable to that in Fontana, California (Lee et al., 2017).

296 The finding reveals that significant fractions of aerosol species were externally mixed

297 with rBC. Individually, sulfate captured by rBC only represented 7.4 (± 2.2)% of NR-

298 PM$_1$ sulfate, similar to the earlier results (Lee et al., 2017;Wang et al., 2020a;Cao et al.,

299 2022;Ma et al., 2020); mass fractions of rBCc nitrate (20.1 ± 5.2%) and chloride (20.4

300 ± 5.5%) in NR-PM$_1$ were similar to the portion of total rBC$_C$ (19.1 ± 4.9%), while the

301 fraction of organics was higher (26.1 ± 7.3%). The lower fraction of sulfate in rBCc

302 than nitrate was likely due to a few reasons. One probable reason is traffic was a

303 dominant source of rBC (see Section 3.2.1 for details) and NO$_2$ is known to be mainly

304 from traffic as well, therefore secondarily formed nitrate was easy to condense on co-

305 emitted rBC, however SO$_2$ is mainly from other sources rather than traffic. Another

306 possible cause is that rBC concentration was relatively high during nighttime, and

307 nighttime formation of nitrate was significant; Sulfate, on the other hand, was mostly

308 formed in the afternoon due to photochemical oxidation in this study (see Section 3.3.2

309 for details), whereas afternoon rBC concentration was low. The relatively high ratio of

310 organics was attributed to the fact that majority of POA species were coated on rBC

311 (average ratio of 72.7 ± 21.0%), while rBC-related SOA was 21.8 (± 7.7)% of the total.

312 Note the rBCc POA here included all four POA factors, and COA$_{NR-PM1}$ did not coat on

313 rBC thus was not included in the calculation.

314

315   **3.2 Distinctive sources of OA in rBCc and in NR-PM$_1$**

316   As shown previously, source apportionment results of OA in rBCc and NR-PM$_1$

317 were different. This section discusses in details the characteristics of OA sources in

318 rBCc and in bulk NR-PM$_1$.

3.2.1 Source apportionment of OA in *r*BCc

Figure 3 shows the HRMS and temporal variations of the six OA factors resolved from PMF analysis of *r*BCc organics. Note the PMF analysis included *r*BC signals (i.e., C_x^+ ions) to aid identification of different factors, yet calculations of elemental ratios of these OA factors did not include C_x^+ ions in order to explicitly explore the properties of organic coating. The HRMS of HOA-rich and *r*BC-rich were similar to the OA previously reported in urban environments near traffic emissions and/or in gasoline/diesel vehicle exhaust (Massoli et al., 2012;Lee et al., 2015;Enroth et al., 2016;Saarikoski et al., 2016;Willis et al., 2016;Lee et al., 2017), therefore both factors were traffic-related. The HOA-rich mass spectrum was featured by intense hydrocarbon ion series (i.e., $C_nH_{2n+1}^+$ and $C_nH_{2n-1}^+$ ions in Fig. 3c), and a lowest O/C ratio of 0.07. Mass fraction of *r*BC signals (i.e., C_n^+ ions, such as *m/z* 12, 24, 36, 48, and 60, etc.) in HOA-rich was 8.1%. Mass spectrum of *r*BC-rich factor had remarkable contribution from *r*BC (24.2%). Beside C_n^+ ions, the *r*BC-rich factor contained more oxygenated organic fragments and presented a higher O/C ratio of 0.21 than that of HOA-rich, similar to previous studies (Willis et al., 2016;Lee et al., 2017). This result is reasonable as previous studies (Corbin et al., 2014;Malmborg et al., 2017) found that refractory organics could generate oxygenated ion fragments (such as CO^+ and CO_2^+ derived from oxygenated species on soot surface or inside soot nanostructure). HOA-rich factor correlated very well with the common AMS tracer of vehicular OA, $C_4H_9^+$ (*r*=0.95, Fig. 3i), while *r*BC-rich factor did match the variation of *r*BC well (*r*=0.90, Fig. 3g). Since diesel combustion often releases more *r*BC than that of gasoline, it is likely that the *r*BC-rich factor is representative of diesel vehicle exhaust while HOA-rich factor represents gasoline combustion emissions. This result demonstrates that laser-only SP-AMS is capable of distinguishing diesel and gasoline burning particles which typically cannot be separated by other AMS measurements. Further verification should be subject of future work.

In this work, a multiple linear regression for the three-dimension size-resolved mass spectra according to the method provided in Ulbrich et al. (2012) was used to resolve the average size distributions of six OA factors. The diagnostic plots are shown

349   in Fig. 4. Overall, the lumped size distribution of six OA factor could reproduce well

350   that of total OA (except for a few size bins, most deviations are within 10%).

351   Correlation between measured and reconstructed OA of all size bins was very tight with

352   r of 0.99 and a slope of 0.97, indicating the robustness of the regressed size distributions

353   of all OA factors. The results together with size distributions of rBCc components, and

354   corresponding mass fractional contributions of different components in all size bins are

355   illustrated in Fig. 5. The average HOA-rich size distribution peaked around 150 nm

356   (D_{va}, vacuum aerodynamic diameter), generally matching with previously reported size

357   distribution of HOA (Sun et al., 2012;Ulbrich et al., 2012;Zhou et al., 2016).

358   Interestingly, size distribution of rBC-rich factor presented two modes, with one

359   peaking ~260 nm, and a more pronounced one peaking ~580 nm (Fig. 5a).

360   The BBOA was identified owing to its obviously higher signals of $C_2H_4O_2^+$ (2.03%)

361   and $C_3H_5O_2^+$ (1.62%) than those in other factors, as these two ions are well-known AMS

362   fragments of the biomass burning tracer, levoglucosan (Mohr et al., 2009;Cubison et

363   al., 2011). The time series of BBOA correlated particularly tightly with both marker

364   ions (r of 0.86 and 0.80, respectively); it in fact also correlated well with K^+ (r=0.79),

365   another tracer of biomass burning emission. The O/C and H/C ratios of BBOA were

366   0.12 and 1.78, and C_n^+ ions accounted for 9.1% of BBOA, all suggesting that the factor

367   was fresh and might be co-emitted with rBC. A relatively high N/C ratio (0.033) was

368   found for BBOA, which could be attributed to the large amounts of nitrogen-containing

369   organic species enriched in biomass burning OA (Laskin et al., 2009). In addition, the

370   size distribution of BBOA (Fig. 5a) (peak size ~500 nm) was similar to that of biomass

371   burning BC-containing particles obtained using single particle mass spectrometry in

372   Shanghai (Gong et al., 2016).

373   The PMF analysis deconvoluted a unique OA factor coated on rBC, namely WS-

374   HOA. Firstly, the WS-HOA mass spectrum had a series of hydrocarbon ion fragments

375   and its time series correlated well with them (e.g., r of 0.90 and 0.92 for WS-HOA vs.

376    $C_4H_7^+$ and $C_4H_9^+$, respectively). Secondly, this factor correlated the best (r=0.57) with

377   aerosol liquid water content (ALWC) (Fig. 3j) compared with the other five OA factors

378   (all r<0.2). Thirdly, a previous study (Ye et al., 2017) that investigated specially the

water-soluble fraction of OA via PMF analysis, separated also a HOA factor that contained significant nitrogen-containing organic fragments, with a highest N/C ratio among all other factors, and correlated well those nitrogenated fragments. The WS-HOA defined here showed similar characteristics with the highest N/C (0.037) among all factors and tight correlations with nitrogen-containing fragments ($r>0.80$). At last, although WS-HOA had a relatively high O/C (0.31) with remarkable contributions from $C_2H_3O^+$ and CO_2^+, yet its correlations with these two ions were in fact not strong (r of 0.46 and 0.44, respectively); and WS-HOA had the least fraction of rBC fragments (0.9%) (note rBC is hydrophobic), even less than the two SOAs (Fig. 3d). Both results suggest that this factor is a collection of water-soluble primary OA species. The peak of WS-HOA size distribution was ~150 nm, close to that of HOA-rich (Figs. 5a). Aqueous-phase processed SOA (aqSOA) were typically with very high O/C ratio (Xu et al., 2019), and size distribution of aqSOA often presented a droplet mode, peaking in relatively large sizes (such as 500~600 nm)(Gilardoni et al., 2016;Wang et al., 2021;Ge et al., 2012). Therefore, the moderate O/C (0.31) and small mode size of WS-HOA again manifest it was not from aqueous-phase reactions but more likely the water-soluble fraction of POA.

The PMF analyses separated two SOA factors, LO-OOA$_{r\text{BC}}$ and MO-OOA$_{r\text{BC}}$. Mass spectral features of the two SOAs were consistent with previous studies: The LO-OOA$_{r\text{BC}}$ was rich in $C_xH_yO_1^+$ ions (38.7%) (such as $C_2H_3O^+$ at m/z 43) but with less contribution from $C_xH_yO_2^+$ ions (7.6%) and an overall moderate O/C (0.25), while MO-OOA$_{r\text{BC}}$ had much more contribution from $C_xH_yO_2^+$ ion family (22.7%) (such as CO_2^+ at m/z 44) and $C_xH_yO_1^+$ ions (44.7%), with a high O/C ratio (0.56). In addition, LO-OOA$_{r\text{BC}}$ correlated better with nitrate ($r=0.83$) than it with sulfate ($r=0.69$), while the correlation between MO-OOA$_{r\text{BC}}$ and sulfate ($r=0.84$) is better than it with nitrate ($r=0.76$). Size distributions of the two SOAs were also in accord with their secondary behaviors, both accumulating at larger sizes (~450 nm for LO-OOA$_{r\text{BC}}$, and a bit larger mode size of ~500 nm for MO-OOA$_{r\text{BC}}$), in agreement with previous observations (Sun et al., 2012;Ulbrich et al., 2012;Zhou et al., 2016).

In total, traffic-related POA (sum of HOA-rich, rBC-rich and WS-HOA) was the

409   most abundant source of rBCc organics (39.1%); BBOA occupied ~18.4%; the

410   contributions of two SOAs were on par with each other (20.2% for LO-OOA$_{r\text{BC}}$, and

411   22.3% for MO-OOA$_{r\text{BC}}$) (Fig. 2g). Among traffic POA, gasoline derived HOA-rich

412   factor outweighed the diesel derived rBC-rich factor (11.4% *vs.* 6.3% of the total rBCc).

413   Contributions of different factors varied greatly for different sizes of rBCc particles

414   (Fig. 5b). Small-sized particles were overwhelmingly dominated by traffic POA; SOA

415   contributions increased with increase of size, and dominated over POA for 300-800 nm

416   ones; contribution of BBOA was also relative larger for 300-800 nm than for other-

417   sized ones; the very large particles (800-1000 nm) were found to be affected mainly by

418   traffic POA in this work. Correspondingly, for the total rBCc particles, rBC cores

419   peaked at ~170 nm, while other secondary inorganic components, behaving like SOA

420   factors, all peaked at a big size (~550 nm) (Fig. 5c) and their mass percentages were

421   also large for large-sized particles (Fig. 5d).

422   Figure 6a further demonstrates the changes of mass fractions of each rBCc

423   component as a function of R_{BC}. R_{BC} is a proxy of coating thickness. It was found that

424   the thinly coated rBCc ($R_{\text{BC}}<3$) were dominated (up to ~80%) by traffic-related POA.

425   With the increase of R_{BC}, contribution of secondary components increased gradually,

426   especially the two SOAs and nitrate (sulfate showed little changes across the whole R_{BC}

427   range); SOA and nitrate contributions reached 40.2% and 31.3% at $R_{\text{BC}} = 8$, respectively.

428   Accordingly, the oxidation degree (OSc = 2*O/C-H/C) (Kroll et al., 2011) of coated

429   organics increased with R_{BC}. In Fig. 6b, we presented the mass contributions of OA

430   factors to the rBC mass at different R_{BC} values. The rBC was as expected,

431   predominantly associated with POA (from 94% at $R_{\text{BC}}<2$ to 66% at $R_{\text{BC}}>8$), similar to

432   those from Fontana (Lee et al., 2017). Contribution of rBC-rich factor decreased

433   obviously, and those of SOA factors increased with R_{BC}. The contributions of HOA-

434   rich, WS-HOA and BBOA factors changed little.

435

436   **3.2.2 Comparisons with NR-PM$_1$ organics**

437   As shown in Fig. S4, PMF analysis separated four OA factor for NR-PM$_1$ organics.

438   Two SOA factors (LO-OOA and MO-OOA) were resolved for both rBCc and NR-PM$_1$,

and their contributions to them were also close (Figs. 2g and 2h). Correlations of time series between the two LO-OOA factors and between the two MO-OOA factors were also tight (*r* of 0.94 and 0.90, respectively), indicating similar formation processes for each SOA. But, of course, the SOAs from *r*BCc and from NR-PM$_1$ were not entirely the same, as later ones had higher O/C ratios (0.52 of LO-OOA$_{NR-PM1}$ and 0.62 of MO-OOA$_{NR-PM1}$). On average, the portion of LO-OOA coated on *r*BC took up 21.6% mass of LO-OOA in total NR-PM$_1$, and the portion was 26.0% for MO-OOA. This result suggests that there were some differences regarding the partitioning of LO-OOA and MO-OOA onto *r*BCc and non-*r*BC particles.

Compared with SOAs, source apportionment results of POA were quite distinct. Firstly, there was only one HOA factor resolved for NR-PM$_1$, while three HOA factors were separated for *r*BCc. Note the *r*BC-rich and WS-HOA factors occupied merely 3.1% and 2.1% of NR-PM$_1$ OA mass, respectively, probably the cause that they were not identified in NR-PM$_1$ OA. Nevertheless, mass loadings of the sum of HOA-rich, *r*BC-rich and WS-HOA factors (termed as HOA$_{rBC}$) agreed quite well with that of HOA$_{NR-PM1}$ (*r*=0.95) (Fig. 7a), verifying both source apportionment results. And, HOA$_{rBC}$ took up 63.7% of HOA$_{NR-PM1}$, while previous studies reported that 81% (Massoli et al., 2012) and 87 % (Massoli et al., 2015) of HOA were associated with *r*BC. These results imply that HOA species in NR-PM$_1$ were largely internally mixed with *r*BC affected by vehicular emissions. Secondly, COA$_{NR-PM1}$ was only identified in NR-PM$_1$ OA. AMS-resolved COA$_{NR-PM1}$ is mainly from cooking oil and food ingredients, therefore it negligibly internally mixes with *r*BC. This result is consistent with previous observations (Lee et al., 2015;Willis et al., 2016;Lee et al., 2017;Collier et al., 2018). At last, BBOA was identified in *r*BCc OA but not in NR-PM$_1$ OA. One plausible reason was that the BBOA mass contribution was minor (equivalent to <5% of NR-PM$_1$ OA mass) therefore was not able to be separated from other OA factors; another speculation is that laser only SP-AMS can detect refractory species that HR-AMS cannot, and a portion of these refractory species are likely rich in biomass burning OA. Identification of BBOA in *r*BCc rather than in simultaneously measured total NR-PM$_1$ was also found in Tibet (Wang et al., 2017) and Beijing (Wang et al., 2020a), role

469 of such BBOA and its interplay with rBC core remain a subject of future work.

470   Diurnal cycles of the POA and SOA factors from both PMF analyses are compared

471 in Figs. 7b and 7c. The diurnal pattern of stacked HOA$_{r$BC}$ indeed agreed with that of

472 HOA$_{NR-PM1}$, both with two peaks in the morning and evening rush hours, and, the

473 patterns of rBC-rich, HOA-rich, and WS-HOA factors showed similar behaviors

474 individually (Fig. 7b). The diurnal variation of COA$_{NR-PM1}$ had pronounced peaks

475 during lunch and dinner times, and its percentage in NR-PM$_1$ OA reached 54% at night.

476 Diurnal patterns of two LO-OOA factors were somewhat different (r=0.35). LO-

477 OOA$_{r$BC}$ has a major peak in the afternoon, while though LO-OOA$_{NR-PM1}$ concentration

478 rose in the afternoon too but peaked in early evening (~20:00). The daily variations of

479 two MO-OOA factors were similar (r=0.83), both peaking at 16:00. The afternoon

480 increases of both SOAs indicate an important role of photochemical reactions, yet

481 differences in formation mechanisms, volatilities and partitioning behaviors of SOA

482 products could lead to diversities of their diurnal patterns and HRMS.

483

484 **3.3 Evolution and formation rBCc components**

485 **3.3.1 Behaviors of rBC cores**

486   Size distribution of rBC cores shown in Fig. 5c was relatively wide. Beside the

487 main peak at ~170 nm, it extended significantly into large sizes and had a small peak at

488 ~550 nm, which was close to the peak of secondary components. With results shown in

489 Fig. 5a, we found that small rBC cores were often thinly coated, while thickly coated

490 rBCc particle were often highly aged and a portion of them also had large-sized rBC

491 cores. This result is likely owing to that oxidation of rBC-bounded organics and/or

492 condensation of secondary species onto rBC surface can induce restructuring of soot

493 aggregates to form compact and large cores (Chen et al., 2018;Chen et al., 2016). Such

494 phenomenon is in line with earlier studies (Liu et al., 2019;Gong et al., 2016). We

495 further show the image plot of size distributions of rBC at different R_{BC} in Fig. S6a. It

496 can be found that the rBC mass in a large part concentrated in particles with R_{BC} of 5-

497 8, and there was indeed a significant portion of rBC appearing in large size range (400-

498 800 nm) with very thick coating (R_{BC} of 8-9).

499

3.3.2 Formation of inorganic salts

Sulfate and nitrate both peaked at a big size ~550 nm (Fig. 5c) and were mainly associated with thickly coated rBCc (R_{BC}>6, Figs. S6d and S6e). To investigate the impacts of photochemistry and aqueous/heterogeneous chemistry on the formation of rBC$_{CT}$ species, we plotted the image plots of size distributions of nitrate, sulfate and organics versus O_X ($O_3 + NO_2$) and relative humidity (RH) in Fig. 8. Here O_X is used as a proxy of photochemical activity (Xu et al., 2017), and RH is an indicator of aqueous reactions (Wu et al., 2018). Nitrate significantly concentrated in 65-100 ppb O_X range but there was a weak accumulation in low O_X as well (Fig. 8a), while in Fig. 8d, nitrate had a prominent hotspot in RH>85%. Generally, both strong photochemical activity and high RH could promote nitrate formation. For sulfate, although the distribution was scattered due to low level of mass loadings, high Ox level seemed to favor sulfate formation (Fig. 8b); sulfate was scattered in the whole RH range and there were some enhancements at high RH (>80%) but was much less clear-cut (Fig. 8e). Therefore aqueous-phase production of sulfate was not important in this campaign.

We further calculated the sulfur oxidation ratio (SOR) and nitrogen oxidation ratio (NOR) (Xu et al., 2014), and plotted their variations against O_X and RH in Figs. 9a and 9e, respectively. The NOR rose substantially at O_X >60 ppb but showed no increase at O_X < 60 ppb, while it increased continuously with RH. Mass ratio of nitrate to rBC stayed at a high level during nighttime when RH was high as well (overall diurnal trend of NO_3^-/rBC was similar to that of RH, see Figs. S7a and S7d). This result indicates a likely more important role of nocturnal nitrate formation (N_2O_5 hydrolysis) (Pathak et al., 2011) (Sun et al., 2011) than photochemical production of nitrate during this campaign; moreover, low temperature and high RH favor nitrate partitioning into the particle phase during nighttime too (Gao et al., 2011). For sulfate, The SOR increased with O_X while it increased with RH under relatively dry conditions (<60%) but decreased with RH when RH>60%. This result, on the other hand, highlights that photochemical production is more important than aqueous/heterogenous formation for sulfate. In addition, mass ratios of sulfate to rBC were enhanced remarkably during

529 daytime and peaked in the afternoon (Fig. S7e), supporting the key role of

530 photochemical formation of sulfate. Sulfate precursor SO_2 was at a high level during

531 daytime too. The main formation pathway of sulfate is strikingly different from that

532 observed in winter Nanjing (Wu et al., 2018), suggesting significant seasonal variability

533 of sulfate formation even in the same region.

534

535 3.3.3 Evolution of organics

536 Organics had a broad average size distribution (Fig. 5c), but unlike rBC, its main

537 peak appeared at 500~600 nm. Figure S6b shows that the majority of organics

538 partitioned in rBCc with R_{BC} of 5.0-9.0 and wide size coverage (300-800 nm).

539 Regarding its dependences on O_X and RH, it mainly accumulated at O_X>70 ppb (Fig.

540 8c) and very high RH (~90%) (Fig. 8f). Consistently, O/C ratio and OSc both peaked

541 in the afternoon (Fig. S7b), all suggesting a critical role of photochemistry in affecting

542 the behavior of organics.

543 Figure 9 illustrates the mass ratios of each OA factor to rBC varying with O_X and

544 RH. Mass ratios of all four POA factors generally presented decreasing trends (despite

545 some fluctuations) against O_X (Fig. 9b), and the total POA_{rBC} showed evident decrease

546 with increase of O_X (Fig. 9d). Instead, both $LO\text{-}OOA_{rBC}$ and $MO\text{-}OOA_{rBC}$, as well as

547 their sum (SOA_{rBC}) increased continuously with O_X (Figs. 9c and 9d). This result proves

548 that photochemical oxidation contributed significantly to both $LO\text{-}OOA_{rBC}$ and MO-

549 OOA_{rBC} formations. Comparatively, decreases of POA_{rBC} perhaps point to its reaction

550 loss upon photochemical oxidation. With regard to RH, besides WS-HOA, the other

551 three POA_{rBC} factors showed almost no dependences on RH (Fig. 9f); note the increase

552 of WS-HOA with RH did not indicate the aqueous production of WS-HOA (see

553 discussion in Section 3.2.1), but a result of enhanced dissolution with increase of

554 moisture. Overall small increase of POA_{rBC} (Fig. 9h) with RH then mainly attributed to

555 WS-HOA. Contrary to the trends with O_X, mass ratios of two SOA factors as well as

556 the total SOA to rBC went down with increase of RH (Figs. 9g and 9h), indicating a

557 trivial role of aqueous/heterogenous oxidation for the SOA coated on rBC observed

558 during this campaign.

559   The aging of OA is generally characterized by the increase of O/C and decrease of

560   H/C (Ng et al., 2011;Zhao et al., 2019).The different aging pathways of OA follow

561   different slopes in the Van Krevelen (VK) diagram (Heald et al., 2010). For example,

562   addition of only one oxygen atom to the carbon skeleton results in a slope equal to 0,

563   while replacement of the hydrogen atom with a carboxylic acid group (−COOH) results

564   in a slope of −1 without fragmentation (C-C bond breaking), and −0.5 with

565   fragmentation (Heald et al., 2010;Ng et al., 2011;Zhao et al., 2019). As presented in Fig.

566   10a, fitting of all OA data yielded a slope of −0.96, very close to −1, suggesting that

567   OA ageing process resembled the hydrogen substitution with a –COOH group

568   (carboxylation). Interestingly, the four OA factors (HOA-rich, WS-HOA, LO-OOA$_{rBC}$

569   and MO-OOA$_{rBC}$) aligned almost in a straight line with a slope of −0.77 (Fig. 10a), also

570   close to −1. Figure S8 further reveals that there was a strong anti-correlation between

571   mass fractions of sum of HOA-rich and WS-HOA and sum of LO-OOA$_{rBC}$ and MO-

572   OOA$_{rBC}$ (r=−0.97); the slope of fitted line was −0.86. All these results suggest that OA

573   evolution may contain a channel of photochemical transformations from HOA-rich and

574   WS-HOA to LO-OOA$_{rBC}$ and then to MO-OOA$_{rBC}$. This result is also in line with the

575   observed decrease of POA$_{rBC}$ and increase of SOA$_{rBC}$ against O$_X$.

576   CHO$^+$, CHO$_2^+$ and C$_2$H$_2$O$_2^+$ are the AMS tracer ions for carbonyl, carboxylic acid

577   and glyoxal, respectively (Wang et al., 2020b;Canagaratna et al., 2015a;Yu et al., 2014).

578   Mass fractions of these three fragment ions presented decreasing trends (or no clear

579   trends) against RH (Fig. S9), suggesting again that aqueous processing is not an

580   important pathway in OA evolution during this campaign. Conversely, fractional

581   contributions of these three ions presented increasing trends versus O$_X$, supporting the

582   dominance of photochemical oxidation pathway (Figs. 10b-d). Figures 10e-g show the

583   scatter plots of H/C versus O/C at different O$_X$ concentrations. The regressed slope was

584   −1.03 for low O$_X$ (<60 ppb) conditions (Fig. 10e), indicating that the OA aging at low

585   O$_X$ level is mainly analogue to the carboxylation process. This result corresponds

586   precisely to the fact that mass fractions of CHO$_2^+$ and C$_2$H$_2$O$_2^+$ increased gradually with

587   O$_X$ at low O$_X$, whereas that of CHO$^+$ remained essentially unchanged (Figs. 10e-g). The

588   fitted slope was −1.14 for moderate O$_X$ conditions (60-80 ppb), and it changed to −0.43

589   for high O_X level (>80 ppb) but correlation became weaker ($r=-0.57$). This result

590   implies that the OA evolution under high O_X conditions might include oxidations by

591   the additions of alcohols, peroxides and carboxylation. In all, the evolution of rBCc OA

592   in Shanghai during this campaign is governed by photochemistry rather than aqueous

593   chemistry, but with different oxidation pathways at different O_X levels.

594   **3.3.4 Coating time of secondary species onto rBC**

595   Although the rBCc organics was dominated by primary sources (Fig. 2g), the

596   diurnal variations of OSc, O/C and H/C of the total organics, were controlled

597   predominantly by the two SOA factors. Correlations between the diurnal cycles of MO-

598   OOA$_{r$BC$}$/rBC and OSc were extremely well ($r=0.97$ with OS_C and $r=0.98$ with O/C),

599   and those of LO-OOA/rBC were also tight ($r=0.91$ with OS_C and $r=0.92$ with O/C).

600   The correlations with LO-OOA$_{r$BC$}$ were a bit weaker than those of MO-OOA$_{r$BC$}$,

601   indicating that MO-OOA$_{r$BC$}$ was probably the final products and was more important

602   in governing the overall oxidation level of organic coating. Figure 11a depicts the

603   diurnal variations of SOA$_{r$BC$}$/rBC and POA$_{r$BC$}$/rBC. Diurnal variations of POA$_{r$BC$}$/rBC

604   and rBC were overall similar, while the daily pattern of SOA$_{r$BC$}$/rBC was almost

605   opposite to that of rBC. This result likely indicates that most POA$_{r$BC$}$ species were co-

606   emitted and coated on rBC cores originally, therefore the coating process during rBCc

607   lifecycle was mainly relevant with SOA species rather than POA species. This process

608   is mainly through photochemical reactions, including in-situ oxidation of originally

609   coated POA species (for example, oxidation of HOA-rich plus WS-HOA to LO-

610   OOA$_{r$BC$}$, then to MO-OOA$_{r$BC$}$), and partitioning of secondary species formed in gas-

611   phase reactions onto rBC surface. In addition, sulfate and nitrate were both secondarily

612   formed, but sulfate was dominated by photochemical production while nitrate was

613   governed by nocturnal heterogenous formation (as discussed in Section 3.3.2); different

614   diurnal patterns of them (Fig. S7) point to different coating processes too.

615   In this regard, we hereby propose a concept of average coating time (ACT), which

616   is used to roughly estimate the timescales required for secondary components coated

617   onto rBC. The specific method is listed as follows:

618   1. Move forward the diurnal variation of SA$_{r$BC$}$/rBC (SA represents a secondary

aerosol species) for n hours to get a new SA_{rBC}/rBC diurnal pattern, labelled as "$SA_{rBC}/rBC(r$-nh-ahead)". Here, the r value is the linear correlation coefficient between the new SA_{rBC}/rBC diurnal pattern with that of rBC.

2. Choose the best correlation coefficient (r-nh-ahead), and nh corresponds to the ACT for this secondary component.

Diurnal patterns of LO-OOA$_{rBC}/rBC$ and MO-OOA$_{rBC}/rBC$ are depicted in Fig. 11b. They were both opposite to the trend of rBC, and they were similar to each other, except that MO-OOA$_{rBC}/rBC$ peaked hours later in the afternoon, signifying that the MO-OOA$_{rBC}$ needs longer time to coated on rBC than LO-OOA$_{rBC}$ does, consistent with the fact that MO-OOA$_{rBC}$ was "more aged". Correspondingly, we obtained an ACT of 7 hours for MO-OOA$_{rBC}$ (*0.35*-*7*h-ahead) and 5 hours for LO-OOA $_{rBC}$ (*0.57*-*5*h-ahead) (Fig. 11c) using the method described above. The ACT of sulfate (*0.65*-*7*h-ahead) and nitrate (*0.30*-*19*h-ahead) were 7 and 19 hours, respectively (Fig. 11d). The results suggest that the rBC emitted mainly in the morning rush hours requires a few hours to be adequately coated by LO-OOA$_{rBC}$, MO-OOA$_{rBC}$ and sulfate, as these three species are mainly produced in the afternoon by photochemical reactions; while photochemical production of nitrate is insignificant, thus rBC was coated by nitrate until later night when nitrate was formed efficiently by heterogenous N_2O_5 hydrolysis. Note the best r values were not high (for example, 0.35 for MO-OOA$_{rBC}$ and 0.30 for nitrate), yet the adjusted trends of all secondary components (Figs. 11c and 11d) matched that of rBC quite well during 3:00~12:00 (r of 0.90, 0.91, 0.84 and 0.84 for MO-OOA$_{rBC}$, LO-OOA$_{rBC}$, sulfate and nitrate, respectively), likely meaning that daytime variations of two SOAs and sulfate were indeed controlled by the coating process while governing factors of their nighttime variations might be complex, and *vice versa* for nitrate.

3.4 Size-resolved hygroscopicity of $rBCc$

By using the method in Section 2.3, we calculated the size-resolved hygroscopicity parameters for the total $rBCc$ (κ_{rBCc}) and the coatings materials (κ_{CT}) across the whole campaign. The image plots are illustrated in Figs. 12a and b. Generally, large κ_{rBCc} and κ_{CT} values occurred at big particle sizes, and this result was overall similar to that in

649 Nanjing during winter (Wu et al., 2019). We further illustrate the size-resolved κ_{rBCc} as

650 a function of R_{BC} in Fig. 12c. The figure shows that κ_{rBCc} overall became larger with

651 increasing particle size regardless of the coating thickness. However, there were some

652 (though not significant) relatively high κ_{rBCc} values in the range of 80-150 nm (bottom

653 left and bottom right in Fig. 12c).

654   In Figs. 13a and b, we further determined the average size-resolved κ_{rBCc} and κ_{CT}

655 as a function of coated diameter (D_{rBCc}). Both κ_{rBCc} and κ_{CT} values were relatively high

656 at D_{rBCc}<100 nm and presented slight decreases from 100 to 150 nm. This is distinctive

657 from those observed in Nanjing, where κ_{CT} increased with D_{rBCc} from 50 nm (Wu et al.,

658 2019). From Figs. 5b and 5d, it can be seen the rBCc with D_{rBCc}<150 nm was dominated

659 by a portion of ammonium and sulfate (8-10%) and organics (~60%), of which organics

660 was dominated by WS-HOA. Such composition explains the relatively high

661 hygroscopicity at D_{rBCc}<150 nm as both ammonium sulfate and WS-HOA are

662 hydrophilic; a slight decrease of the hygroscopicity from 100 to 150 nm D_{rBCc} was also

663 a response of decreased mass contributions of ammonium sulfate and WS-HOA (and

664 increase of hydrophobic HOA-rich contribution).

665   Figures 13a and b provide the fitted exponential functions for the mean κ_{rBCc} and

666 κ_{CT} with D_{rBCc}. The equations are: $\kappa_{rBCc}(x)= 0.29-0.14 \times \exp(-0.006 \times x)$ and $\kappa_{CT}(x) =$

667 $0.35 - 0.09 \times \exp(-0.003 \times x)$ (x is D_{rBCc}, 150<x<1000 nm). Here, 0.29 and 0.35 are

668 the upper limits of κ_{rBCc} and κ_{CT}, higher than those reported in Nanjing (0.28 and 0.30

669 for κ_{rBCc} and κ_{CT}); yet the increasing rates of κ_{rBCc} and κ_{CT} with D_{rBCc} are 0.14 and 0.09,

670 respectively, which are much lower than those from Nanjing (0.35 and 0.27 for κ_{rBCc}

671 and κ_{CT})(Wu et al., 2019). Smaller increased contributions of hydrophilic secondary

672 species from 150 to 1000 nm in Shanghai than those from 100 to 1000 nm in Nanjing

673 are likely the cause of smaller increasing rates of hygroscopicity parameters. In addition,

674 it should be noted that the hygroscopicity is not only determined by the bulk

675 composition, but also affected by the phase state of particles. For instance, a recent

676 study reveals that the hygroscopic growth of phase-separated particles (with ammonium

677 sulfate as cores) can be reduced by the secondary organic shells and is dependent on

678 the thickness of organic coating (Li et al., 2021).

679   The critical supersaturation (SS_C) for a selected dry diameter (D_{rBCc} measured by

680   SP-AMS) of a rBCc particle with a hygroscopicity parameter κ_{rBCc}, can be calculated

681   by the "κ-Kohler theory" equation (Petters and Kreidenweis, 2007). Based on the size-

682   resolved κ_{rBCc}, the CCN activation diameter (D_{50}) of particles at a given critical SS_C can

683   be calculated (Wu et al., 2019). Then, by combining the measured rBCc number size

684   distribution and the D_{50} value, activation fraction (f_{AC}) of rBCc number population (i.e.,

685   the fraction greater than the D_{50}) can be obtained. Figure 13c shows the SS_C as a

686   function of D_{rBCc} for the entire sampling period to obtain the D_{50} at a specific SS_C. The

687   D_{50} values of the rBCc particles were determined to be 166 ($\pm$ 16) nm and 110 ($\pm$ 5) nm

688   for SS_C of 0.1% and 0.2%, respectively. The two D_{50} values are both smaller than those

689   determined for rBCc particle in Nanjing (Wu et al., 2019), likely owing to the presence

690   of WS-HOA in Shanghai. Figure 13d shows the f_{AC} at SS_C of 0.1% (D_{50} of 166 nm) was

691   16 ($\pm$ 3)%, and the f_{AC} at SS_C of 0.2% (D_{50} of 110 nm) was 59 ($\pm$ 4)%.

692

693   **3.5 A case study influenced by ship emissions**

694   **3.5.1 Potential source areas of rBCc**

695   To explore the potential geographic origins of rBCc at the receptor site, the hybrid

696   single-particle Lagrangian integrated trajectory (HYSPLIT) model (version 4.9) was

697   applied here. Figure 14a shows that the backward trajectories were classified into four

698   air mass clusters, including one long-range transport from northern sea (Cluster1), one

699   long-range transport from northeastern sea (Cluster2), a local one from eastern ports

700   (Cluster3), and one from northwestern inland region (Cluster4). The four clusters

701   occupied 23.8%, 33.8%, 37.3%, and 5.0% of the total trajectories, respectively. It is

702   clear that the sampling period was influenced by offshore air masses in most of the time

703   (95%). Cluster3 had the highest mean rBCc concentrations (13.2 $\pm$ 10.9 μg m^{-3}) while

704   the mean concentrations of the other three clusters were apparently lower (4.3~5.2 μg

705   m^{-3}). This result is plausible as Cluster3 was the shortest in length therefore was least

706   diluted compared with other three clusters. Average chemical compositions of the rBCc

707   from four clusters (Fig. 14b) showed some differences as well: Cluster1 and Cluster2

708   had higher MO-OOA$_{rBC}$ contributions, possibly owing to the interceptions of more

709 aged SOA species during the long-range transports; While Cluster4 had less MO-

710 OOA$_{rBC}$ but a bit more POA$_{rBC}$ contributions, likely attributing to more primary species

711 emitted in inland regions (similarly, a higher fraction of nitrate was likely because of

712 enhanced NO_2 emissions).

713

714 **3.5.2 A typical case of *r*BCc affected by ship emissions**

715   Ship emissions are found to have an important impact on the air quality of

716 Shanghai and the Yangtze River Delta (Zhao et al., 2013;Fan et al., 2016;Liu et al.,

717 2017b;Chen et al., 2019). The ship engines usually burn heavy fuel oil (HFO), and

718 vanadium (V) and nickel (Ni) can be adopted as reliable tracers for the ship-emitted

719 particles (Ault et al., 2009;Moldanová et al., 2009;Ault et al., 2010). The long-term

720 variation of Ni/V ratio in ship-emitted particles in Shanghai has been recently reported

721 (Yu et al., 2021). The main conclusion is that Ni/V ratio was close to 0.4 in 2018, while

722 it became to be greater than 2.0 in 2020. Our measurement was carried out in 2018, and

723 we therefore chose a period from November 3rd to 5th as a typical case affected by ship

724 emissions (SEP period), since the average Ni/V ratio was ~0.50 and high concentrations

725 of both Ni and V were found. Figure S10 shows the concentration-weighted trajectories

726 (CWT) of ship emission tracers (V, Ni), *r*BC and *r*BC-rich factor during SEP, displaying

727 that these components were mainly from sea. During SEP, the correlation coefficient (*r*)

728 between V(Ni) and *r*BC was 0.69 (0.74), indicating the SEP was indeed impacted by

729 ship emissions.

730   Figure 15 displays the chemical characteristics of *r*BCc and NR-PM$_1$ components

731 (especially the OA factors), V and Ni, gaseous pollutants and the meteorological

732 parameters during SEP. As a comparison, we also selected a period with no ship

733 emissions with the same time span as SEP (from 0:00 on November 10 to 0:00 on

734 November 12, termed as non-SEP), and a similar plot during non-SEP is presented in

735 Fig. S11. During SEP, the wind was mainly from east, and the average wind speed was

736 ~0.5 (± 0.3) m s^{-1} (Fig. 15a); Wusong, Luojing and Waigaoqiao ports located northeast

737 of the sampling site (Fig. S1). Instead, the wind was mainly from north during non-SEP

738 (Fig. S11a). During SEP, the average mass concentrations of V and Ni were 6.3 (± 3.1)

739   ng m^{-3} and 3.2 (± 1.4) ng m^{-3}, respectively, while those during non-SEP were only 2.9

740   (± 1.4) ng m^{-3} and 2.6 (± 1.6) ng m^{-3}. The average mass ratio of V/Ni during SEP was

741   2.0 in agreement with those reported in ship-influenced PM$_1$ (Mazzei et al., 2008;Mar

742   et al., 2009), and within the range of 1.9 to 3.5 for domestic HFO (Zhao et al., 2013),

743   while the average ratio of V/Ni (1.1± 0.8) during non-SEP was outside the range.

744   Moreover, the major air pollutants emitted from ships include nitrogen oxides (NO$_x$),

745   sulfur oxides (SO$_2$), carbon monoxide (CO), hydrocarbons and primary/secondary

746   particles (Becagli et al., 2017;Wu et al., 2021). As demonstrated in Fig. 15d and Fig.

747   S11d, SO$_2$ concentration was overall higher during SEP (10:00-16:00 on November 11

748   not included); mass loading of NO$_2$ was higher during the rush hours of non-SEP, but

749   was higher at night (no traffic) during SEP. Mass proportion of sulfate in NR-PM$_1$

750   during SEP was also higher than that during non-SEP (22.7 ± 8.1 % *vs.* 19.1± 5.3 %),

751   but *vice versa* for nitrate (17.8 (± 9.9)% during SEP *vs.* 26.2 (± 9.1)% during non-SEP).

752   We further investigated the dependences of *r*BCc and NR-PM$_1$ species on V during

753   SEP and non-SEP, as shown in Fig. S12. Here we only used V since Ni level might be

754   influenced by other emission sources, such as refining industry (Jang et al., 2007;Kim

755   et al., 2014) in urban Shanghai, and during non-SEP, Ni still presented a good

756   correlation with *r*BC (*r*=0.80). During SEP, V concentrations (most of them >4 ng m^{-3})

757   overall positively correlated with both sulfate and nitrate (except for *r*BCc sulfate) (Fig.

758   S12a). Considering that V concentration was independently measured for all fine

759   particles, a better correlation with total NR-PM$_1$ sulfate than it with *r*BCc sulfate is

760   reasonable. Similarly, V-rich particles had positive correlations with traffic-related OA

761   and LO-OOA no matter in *r*BCc or in total NR-PM$_1$ (Fig. S12b). Conversely, during

762   non-SEP, particles with low-V content (most of them <4 ng m^{-3}) had no clear links with

763   sulfate, nitrate, POA and SOA species (even anti-correlations for V>2.5 ng m^{-3}) (Figs.

764   S12c and S12d; a detailed comparison of the correlation coefficients of V with OA

765   factors of *r*BCc and NR-PM$_1$ organics are provided in Table S2). The results above

766   demonstrate that during SEP, chemical properties of the particles (both fresh and aged

767   ones) were clearly linked with ship influences.

768   Previous studies (Ault et al., 2009;Ault et al., 2010;Liu et al., 2017b) have shown

that the fresh ship-emitted V-rich particles are typically accompanied by high sulfate contribution, while those aged V-containing ship particles are on the other hand with relatively high nitrate contribution. In order to further probe chemical characteristics and evolution processes of particles influenced by ship emissions, we divided SEP into three episodes (i.e., EP1-EP3) (marked in Fig. 15). During EP1, rBC content was highest (Fig. 15k) and coating was thinnest (Fig. S13i) indicating the particles were relatively fresh, nevertheless the SOA contents were not low (Figs.15j and 15l), OS_C was moderate (Fig. S13j), sulfate portions in NR-PM$_1$ and rBCc were both the highest (26.5%), and nitrate portion was the lowest (9.8%) among three episodes (Figs.15i and 15k). Such composition is not common in other cases, demonstrating it was a specific period impacted by fresh ship emissions. EP2 had the highest mass loadings of V, gas pollutants as well as the lowest planetary boundary layer (PBL) height (~200 meters) (Fig. S13). Mass contributions of nitrate increased and sulfate decreased, and rBC content decreased from those during EP1, signifying that the particle population likely contained some aged ship-emitted particles. Surely, particle composition during EP2 was also influenced by the formation mechanisms of secondary species: EP2 was mostly during nighttime, therefore photochemical formation of sulfate and SOA were weak (as shown in Figs. 15i and 15l, sulfate contribution was only 15.1%, and SOA contribution was only 33.7%), while nitrate formation was enhanced due to the nocturnal process. During EP3, rBC was the lowest, sulfate and V were moderate, nitrate and SOA were highest in both rBCc and NR-PM$_1$, OS_C and R_{BC} were highest in rBCc among the three episodes (Figs. 15i-l and Figs. S13i-k), therefore it was also a period with influence from aged ship-emitted particles; the difference from EP2 is that photochemically formed sulfate and SOA were still significant as EP3 was in the later afternoon and early evening, though heterogeneously formed nitrate played a non-negligible role too (see the increase of RH, increase of nitrate and decrease of O$_3$ concentrations from the beginning of EP3 in Fig. 15).

4. Conclusions and implications

We conducted a field measurement during November of 2018 in urban Shanghai,

799 China, focusing on the elucidation of physical and chemical properties of the ambient

800 particles containing rBC cores (rBCc) by using a laser-only SP-AMS together with a

801 HR-AMS. The campaign-average rBCc was 4.6 (± 4.4) μg m^{-3}, occupying ~19.1 (±

802 4.9) % mass of the total NR-PM$_1$. The average mass ratio of coating to rBC cores (R_{BC})

803 was ~5.0 (± 1.7), indicating an overall thick coating, compared with the rBCc near

804 combustion source. Sulfate was found to preferentially condense on non-rBC particles

805 thus led to a low fraction of rBCc sulfate to that in NR-PM$_1$ (7.4% ± 2.2 %), while

806 distribution of nitrate between rBCc and non-rBC particles showed no obvious

807 difference. PMF analysis on rBCc and NR-PM$_1$ OA reveals that cooking-related

808 organics were externally mixed with rBC, and a small portion of organics from biomass

809 burning was only present in rBCc; the traffic-related OA species, however, was in a

810 large part internally mixed with rBC.

811 A regression algorithm was applied to deconvolute the size distributions of

812 individual rBCc OA factors, and results show that small rBCc particles were

813 predominantly generated from traffic, and such particles could grow bigger because of

814 condensation of secondary inorganic and organic components, resulting in thick coating.

815 Investigation on diurnal patterns of the rBCc species reveals that sulfate and two SOA

816 factors (LO-OOA$_{rBC}$ and MO-OOA$_{rBC}$) were generated mainly through daytime

817 photochemical oxidation; nitrate, on the other hand, was governed mainly by the

818 nocturnal N$_2$O$_5$ hydrolysis. Partial SOA was found to be produced from in-situ

819 photochemical conversion from traffic-related POA. An average coating time (ACT)

820 was proposed to roughly estimate the timescales for the secondary species to coat on

821 rBC, and the ACT of sulfate, LO-OOA$_{rBC}$, MO-OOA$_{rBC}$ and nitrate were approximately

822 7, 5, 7 and 19 hours, respectively.

823 Moreover, the size-resolved hygroscopicity parameters of rBCc particles (κ_{rBCc})

824 and the coating material (κ_{CT}) were obtained based on the elucidated composition of

825 rBCc particles. The fitted equations are: $\kappa_{rBCc}(x)= 0.29 - 0.14 \times \exp(-0.006 \times x)$ and

826 $\kappa_{CT}(x) = 0.35 - 0.09 \times \exp(-0.003 \times x)$ (x is D_{rBCc}, 150<x<1000 nm). The minimums

827 of both κ_{rBCc} and κ_{CT} were at ~150 nm due to the abundances of hydrophobic rBC cores

828 and traffic-related HOA at this size. Under critical supersaturations (SS_C) of 0.1% and

829   0.2%, the D_{50} values were estimated to be 166 ($\pm$ 16) and 110 ($\pm$ 5) nm, and the

830   activated number fractions of rBCc particles were 16 ($\pm$ 3)% and 59 ($\pm$ 4)%,

831   respectively. Finally, a typical case with influence from ship emissions was investigated.

832   During this period, the rBCc particles were enriched in V (6.3 $\pm$ 3.1 ng m^{-3}), with a

833   V/Ni ratio of 2.0 ($\pm$ 0.6), and various secondary formation processes affect the ship-

834   emitted particles at different times of the day.

835   In summary, the findings from this comprehensive study on rBCc provide rich

836   information regarding the various primary sources and secondary formation pathways

837   of species coated on rBC, as well as the features of distributions of those species

838   between rBC and non-rBC particles. In particular, different types of rBCc particles

839   from diesel and gasoline vehicle emissions were resolved and elucidation of their

840   properties are useful to their future effective control. Understanding of the formation

841   processes and coating timescales of secondary components is helpful to understand the

842   impact of ambient BC particles too. At last, the parameterized relationship of

843   hygroscopicity with size distribution is useful for modelling the climate effect of rBC

844   (alternation of cloud properties).

845

846   *Data availability.* The data in this study are available from the authors upon request

847   (caxinra@163.com).

848

849   *Supplement.* The supplement related to this article is available online at: XXX

850

851   *Author contributions.* SJC, DDH, YZW, JFW, FZS, and XLG conducted the field

852   measurement. SJC, DDH, YZW, JFW, and JKX analyzed the data. YJZ, HLW, CH and

853   HL reviewed the paper and provide useful suggestions. SJC and XLG wrote the paper.

854

855   *Competing interests.* The contact author has declared that neither they nor their co-

856   authors have any competing interests.

857

858   *Disclaimer.* Publisher's note: Copernicus Publications remains neutral with regard to

859 jurisdictional claims in published maps and institutional affiliations.

860

861 *Acknowledgements.* We sincerely thank SAES to provide data of gaseous pollutants and

862 particulate V and Ni, and the logistic help during the campaign.

863

864 *Financial support.* This work has been supported by the National Natural Science

865 Foundation of China (42021004, 21976093 and 21777073).

866

867 *Review statement*. This paper was XXX.

868

869 **References**

870 Aiken, A. C., DeCarlo, P. F., Kroll, J. H., Worsnop, D. R., Huffman, J. A., Docherty,

871 K. S., Ulbrich, I. M., Mohr, C., Kimmel, J. R., Sueper, D., Sun, Y., Zhang, Q., Trimborn,

872 A., Northway, M., Ziemann, P. J., Canagaratna, M. R., Onasch, T. B., Alfarra, M. R.,

873 Prevot, A. S. H., Dommen, J., Duplissy, J., Metzger, A., Baltensperger, U., and Jimenez,

874 J. L.: O/C and OM/OC ratios of primary, secondary, and ambient organic aerosols with

875 high-resolution time-of-flight aerosol mass spectrometry, Environ. Sci. Technol., 42,

876 4478-4485, https://doi.org/10.1021/es703009q, 2008.

877 Ault, A. P., Moore, M. J., Furutani, H., and Prather, K. A.: Impact of emissions

878 from the Los Angeles port region on San Diego air quality during regional transport

879 events, Environ. Sci. Technol., 43, 3500-3506, https://doi.org/10.1021/es8018918,

880 2009.

881 Ault, A. P., Gaston, C. I., Ying, W., Gerardo, D., Thiemens, M. H., and Prather, K.

882 A.: Characterization of the single particle mixing state of individual ship plume events

883 measured at the Port of Los Angeles, Environ. Sci. Technol., 44, 1954-1961,

884 https://doi.org/10.1021/es902985h, 2010.

885 Becagli, S., Anello, F., Bommarito, C., Cassola, F., Calzolai, G., Di Iorio, T., di

886 Sarra, A., Gómez-Amo, J.-L., Lucarelli, F., Marconi, M., Meloni, D., Monteleone, F.,

887 Nava, S., Pace, G., Severi, M., Sferlazzo, D. M., Traversi, R., and Udisti, R.:

888 Constraining the ship contribution to the aerosol of the central Mediterranean, Atmos.

Chem. Phys., 17, 2067-2084, https://doi.org/10.5194/acp-17-2067-2017, 2017.

Bond, T. C., Doherty, S. J., Fahey, D. W., Forster, P. M., Berntsen, T., DeAngelo, B. J., Flanner, M. G., Ghan, S., Kärcher, B., Koch, D., Kinne, S., Kondo, Y., Quinn, P. K., Sarofim, M. C., Schultz, M. G., Schulz, M., Venkataraman, C., Zhang, H., Zhang, S., Bellouin, N., Guttikunda, S. K., Hopke, P. K., Jacobson, M. Z., Kaiser, J. W., Klimont, Z., Lohmann, U., Schwarz, J. P., Shindell, D., Storelvmo, T., Warren, S. G., and Zender, C. S.: Bounding the role of black carbon in the climate system: A scientific assessment, J. Geophys. Res.: Atmos., 118, 5380-5552, https://doi.org/10.1002/jgrd.50171, 2013.

Canagaratna, M. R., Jayne, J. T., Jimenez, J. L., Allan, J. D., Alfarra, M. R., Zhang, Q., Onasch, T. B., Drewnick, F., Coe, H., Middlebrook, A., Delia, A., Williams, L. R., Trimborn, A. M., Northway, M. J., DeCarlo, P. F., Kolb, C. E., Davidovits, P., and Worsnop, D. R.: Chemical and microphysical characterization of ambient aerosols with the aerodyne aerosol mass spectrometer, Mass Spectrom. Rev., 26, 185-222, https://doi.org/10.1002/mas.20115, 2007.

Canagaratna, M. R., Jimenez, J. L., Kroll, J. H., Chen, Q., Kessler, S. H., Massoli, P., Hildebrandt Ruiz, L., Fortner, E., Williams, L. R., Wilson, K. R., Surratt, J. D., Donahue, N. M., Jayne, J. T., and Worsnop, D. R.: Elemental ratio measurements of organic compounds using aerosol mass spectrometry: characterization, improved calibration, and implications, Atmos. Chem. Phys., 15, 253-272, https://doi.org/10.5194/acp-15-253-2015, 2015a.

Canagaratna, M. R., Massoli, P., Browne, E. C., Franklin, J. P., Wilson, K. R., Onasch, T. B., Kirchstetter, T. W., Fortner, E. C., Kolb, C. E., Jayne, J. T., Kroll, J. H., and Worsnop, D. R.: Chemical compositions of black carbon particle cores and coatings via soot particle aerosol mass spectrometry with photoionization and electron ionization, J. Phys. Chem. A, 119, 4589-4599, https://doi.org/10.1021/jp510711u, 2015b.

Cao, L.-M., Wei, J., He, L.-Y., Zeng, H., Li, M.-L., Zhu, Q., Yu, G.-H., and Huang, X.-F.: Aqueous aging of secondary organic aerosol coating onto black carbon: Insights from simultaneous L-ToF-AMS and SP-AMS measurements at an urban site in southern China, J. Clean Prod., 330, 129888,

https://doi.org/10.1016/j.jclepro.2021.129888, 2022.

Cappa, C. D., Onasch, T. B., Massoli, P., Worsnop, D. R., Bates, T. S., Cross, E. S., Davidovits, P., Hakala, J., Hayden, K. L., Jobson, B. T., Kolesar, K. R., Lack, D. A., Lerner, B. M., Li, S.-M., Mellon, D., Nuaaman, I., Olfert, J. S., Petäjä, T., Quinn, P. K., Song, C., Subramanian, R., Williams, E. J., and Zaveri, R. A.: Radiative Absorption Enhancements Due to the Mixing State of Atmospheric Black Carbon, Science, 337, 1078-1081, https://doi.org/10.1126/science.1230260, 2012.

Chang, R. Y. W., Slowik, J. G., Shantz, N. C., Vlasenko, A., Liggio, J., Sjostedt, S. J., Leaitch, W. R., and Abbatt, J. P. D.: The hygroscopicity parameter (κ) of ambient organic aerosol at a field site subject to biogenic and anthropogenic influences: relationship to degree of aerosol oxidation, Atmos. Chem. Phys., 10, 5047-5064, https://doi.org/10.5194/acp-10-5047-2010, 2010.

Chen, B., Bai, Z., Cui, X., Chen, J., Andersson, A., and Gustafsson, O.: Light absorption enhancement of black carbon from urban haze in Northern China winter, Environ. Pollut., 221, 418-426, https://doi.org/10.1016/j.envpol.2016.12.004, 2017.

Chen, C., Fan, X., Shaltout, T., Qiu, C., Ma, Y., Goldman, A., and Khalizov, A. F.: An unexpected restructuring of combustion soot aggregates by subnanometer coatings of polycyclic aromatic hydrocarbons, Geophys. Res. Lett., 43, 11,080-011,088, https://doi.org/10.1002/2016GL070877, 2016.

Chen, C., Enekwizu, O. Y., Fan, X., Dobrzanski, C. D., Ivanova, E. V., Ma, Y., Gor, G. Y., and Khalizov, A. F.: Single Parameter for Predicting the Morphology of Atmospheric Black Carbon, Environ. Sci. Technol., 52, 14169-14179, https://doi.org/10.1021/acs.est.8b04201, 2018.

Chen, D., Tian, X., Lang, J., Zhou, Y., Li, Y., Guo, X., Wang, W., and Liu, B.: The impact of ship emissions on PM2.5 and the deposition of nitrogen and sulfur in Yangtze River Delta, China, Sci. Total Environ., 649, 1609-1619, https://doi.org/10.1016/j.scitotenv.2018.08.313, 2019.

Clegg, S. L., Brimblecombe, P., and Wexler, A. S.: Thermodynamic model of the system H+− NH4+− SO42-− NO3-− H2O at tropospheric temperatures, 102, 2155–2171, https://doi.org/10.1021/jp973043j, 1998.

949   Collier, S., Williams, L. R., Onasch, T. B., Cappa, C. D., Zhang, X., Russell, L.

950   M., Chen, C.-L., Sanchez, K. J., Worsnop, D. R., and Zhang, Q.: Influence of Emissions

951   and Aqueous Processing on Particles Containing Black Carbon in a Polluted Urban

952   Environment: Insights From a Soot Particle-Aerosol Mass Spectrometer, J. Geophys.

953   Res.: Atmos., 123, 6648-6666, https://doi.org/10.1002/2017jd027851, 2018.

954   Corbin, J. C., Sierau, B., Gysel, M., Laborde, M., Keller, A., Kim, J., Petzold, A.,

955   Onasch, T. B., Lohmann, U., and Mensah, A. A.: Mass spectrometry of refractory black

956   carbon particles from six sources: carbon-cluster and oxygenated ions, Atmos. Chem.

957   Phys., 14, 2591-2603, https://doi.org/10.5194/acp-14-2591-2014, 2014.

958   Cubison, M. J., Ortega, A. M., Hayes, P. L., Farmer, D. K., Day, D., Lechner, M.

959   J., Brune, W. H., Apel, E., Diskin, G. S., Fisher, J. A., Fuelberg, H. E., Hecobian, A.,

960   Knapp, D. J., Mikoviny, T., Riemer, D., Sachse, G. W., Sessions, W., Weber, R. J.,

961   Weinheimer, A. J., Wisthaler, A., and Jimenez, J. L.: Effects of aging on organic aerosol

962   from open biomass burning smoke in aircraft and laboratory studies, Atmos. Chem.

963   Phys., 11, 12049-12064, https://doi.org/10.5194/acp-11-12049-2011, 2011.

964   DeCarlo, P. F., Kimmel, J. R., Trimborn, A., Northway, M. J., Jayne, J. T., Aiken,

965   A. C., Gonin, M., Fuhrer, K., Horvath, T., Docherty, K. S., Worsnop, D. R., and Jimenez,

966   J. L.: Field-Deployable, High-Resolution, Time-of-Flight Aerosol Mass Spectrometer,

967   Anal. Chem. , 78, 8281-8289, https://doi.org/10.1021/ac061249n, 2006.

968   Enroth, J., Saarikoski, S., Niemi, J., Kousa, A., Ježek, I., Močnik, G., Carbone, S.,

969   Kuuluvainen, H., Rönkkö, T., Hillamo, R., and Pirjola, L.: Chemical and physical

970   characterization of traffic particles in four different highway environments in the

971   Helsinki   metropolitan   area,   Atmos.   Chem.   Phys.,   16,   5497-5512,

972   https://doi.org/10.5194/acp-16-5497-2016, 2016.

973   Fan, Q., Zhang, Y., Ma, W., Ma, H., Feng, J., Yu, Q., Yang, X., Ng, S. K., Fu, Q.,

974   and Chen, L.: Spatial and Seasonal Dynamics of Ship Emissions over the Yangtze River

975   Delta and East China Sea and Their Potential Environmental Influence, Environ. Sci.

976   Technol., 50, 1322-1329, https://doi.org/10.1021/acs.est.5b03965, 2016.

977   Gao, X., Yang, L., Cheng, S., Gao, R., Zhou, Y., Xue, L., Shou, Y., Wang, J., Wang,

978   X., Nie, W., Xu, P., and Wang, W.: Semi-continuous measurement of water-soluble ions

in PM2.5 in Jinan, China: Temporal variations and source apportionments, Atmos. Environ., 45, 6048-6056, https://doi.org/10.1016/j.atmosenv.2011.07.041, 2011.

Ge, X., Zhang, Q., Sun, Y., Ruehl, C. R., and Setyan, A.: Effect of aqueous-phase processing on aerosol chemistry and size distributions in Fresno, California, during wintertime, Environ. Chem., 9, 221-235, https://doi.org/10.1071/EN11168, 2012.

Gilardoni, S., Massoli, P., Paglione, M., Giulianelli, L., Carbone, C., Rinaldi, M., Decesari, S., Sandrini, S., Costabile, F., Gobbi, G. P., Pietrogrande, M. C., Visentin, M., Scotto, F., Fuzzi, S., and Facchini, M. C.: Direct observation of aqueous secondary organic aerosol from biomass-burning emissions, Proc. Natl. Acad. Sci. U. S. A., 113, 10013-10018, https://doi.org/10.1073/pnas.1602212113, 2016.

Gong, X., Zhang, C., Chen, H., Nizkorodov, S. A., Chen, J., and Yang, X.: Size distribution and mixing state of black carbon particles during a heavy air pollution episode in Shanghai, Atmos. Chem. Phys., 16, 5399-5411, https://doi.org/10.5194/acp-16-5399-2016, 2016.

Gysel, M., Crosier, J., Topping, D. O., Whitehead, J. D., Bower, K. N., Cubison, M. J., Williams, P. I., Flynn, M. J., McFiggans, G. B., and Coe, H.: Closure study between chemical composition and hygroscopic growth of aerosol particles during TORCH2, Atmos. Chem. Phys., 7, 6131-6144, https://doi.org/10.5194/acp-7-6131-2007, 2007.

Heald, C. L., Kroll, J. H., Jimenez, J. L., Docherty, K. S., DeCarlo, P. F., Aiken, A. C., Chen, Q., Martin, S. T., Farmer, D. K., and Artaxo, P.: A simplified description of the evolution of organic aerosol composition in the atmosphere, Geophys. Res. Lett., 37, https://doi.org/10.1029/2010gl042737, 2010.

Hu, D., Liu, D., Kong, S., Zhao, D., Wu, Y., Li, S., Ding, S., Zheng, S., Cheng, Y., Hu, K., Deng, Z., Wu, Y., Tian, P., Liu, Q., Huang, M., and Ding, D.: Direct Quantification of Droplet Activation of Ambient Black Carbon Under Water Supersaturation, J. Geophys. Res.: Atmos., 126, e2021JD034649, https://doi.org/10.1029/2021jd034649, 2021.

Jacobi, H. W., Lim, S., Ménégoz, M., Ginot, P., Laj, P., Bonasoni, P., Stocchi, P., Marinoni, A., and Arnaud, Y.: Black carbon in snow in the upper Himalayan Khumbu

1009   Valley, Nepal: observations and modeling of the impact on snow albedo, melting, and

1010   radiative forcing, The Cryosphere, 9, 1685-1699, https://doi.org/10.5194/tc-9-1685-

1011   2015, 2015.

1012   Jang, H.-N., Seo, Y.-C., Lee, J.-H., Hwang, K.-W., Yoo, J.-I., Sok, C.-H., and Kim,

1013   S.-H.: Formation of fine particles enriched by V and Ni from heavy oil combustion:

1014   Anthropogenic sources and drop-tube furnace experiments, Atmos. Environ., 41, 1053-

1015   1063, https://doi.org/10.1016/j.atmosenv.2006.09.011, 2007.

1016   Jayne, J. T., Leard, D. C., Zhang, X., Davidovits, P., Smith, K. A., Kolb, C. E., and

1017   Worsnop, D. R.: Development of an aerosol mass spectrometer for size and composition

1018   analysis of submicron particles, Aerosol Sci. Technol., 33, 49-70,

1019   https://doi.org/10.1080/027868200410840, 2000.

1020   Kim, K.-H., Shon, Z.-H., Mauulida, P. T., and Song, S.-K.: Long-term monitoring

1021   of airborne nickel (Ni) pollution in association with some potential source processes in

1022   the urban environment, Chemosphere, 111, 312-319,

1023   https://doi.org/10.1016/j.chemosphere.2014.03.138, 2014.

1024   Kroll, J. H., Donahue, N. M., Jimenez, J. L., Kessler, S. H., Canagaratna, M. R.,

1025   Wilson, K. R., Altieri, K. E., Mazzoleni, L. R., Wozniak, A. S., Bluhm, H., Mysak, E.

1026   R., Smith, J. D., Kolb, C. E., and Worsnop, D. R.: Carbon oxidation state as a metric

1027   for describing the chemistry of atmospheric organic aerosol, Nat. Chem., 3, 133-139,

1028   https://doi.org/10.1038/nchem.948, 2011.

1029   Lambe, A. T., Ahern, A. T., Wright, J. P., Croasdale, D. R., Davidovits, P., and

1030   Onasch, T. B.: Oxidative aging and cloud condensation nuclei activation of laboratory

1031   combustion soot, J. Aerosol. Sci., 79, 31-39,

1032   https://doi.org/10.1016/j.jaerosci.2014.10.001, 2015.

1033   Laskin, A., Smith, J. S., and Laskin, J.: Molecular characterization of nitrogen-

1034   containing organic compounds in biomass burning aerosols using high-resolution mass

1035   spectrometry, Environ. Sci. Technol., 43, 3764-3771,

1036   https://doi.org/10.1021/es803456n, 2009.

1037   Lee, A. K. Y., Willis, M. D., Healy, R. M., Onasch, T. B., and Abbatt, J. P. D.:

1038   Mixing state of carbonaceous aerosol in an urban environment: single particle

characterization using the soot particle aerosol mass spectrometer (SP-AMS), Atmos. Chem. Phys., 15, 1823-1841, https://doi.org/10.5194/acp-15-1823-2015, 2015.

Lee, A. K. Y., Chen, C.-L., Liu, J., Price, D. J., Betha, R., Russell, L. M., Zhang, X., and Cappa, C. D.: Formation of secondary organic aerosol coating on black carbon particles near vehicular emissions, Atmos. Chem. Phys., 17, 15055-15067, https://doi.org/10.5194/acp-17-15055-2017, 2017.

Lee, A. K. Y., Rivellini, L. H., Chen, C. L., Liu, J., Price, D. J., Betha, R., Russell, L. M., Zhang, X., and Cappa, C. D.: Influences of primary emission and secondary coating formation on the particle diversity and mixing state of black carbon particles, Environ. Sci. Technol., 53, 9429-9438, https://doi.org/10.1021/acs.est.9b03064, 2019.

Li, W., Teng, X., Chen, X., Liu, L., Xu, L., Zhang, J., Wang, Y., Zhang, Y., and Shi, Z.: Organic coating reduces hygroscopic growth of phase-separated aerosol particles, Environ. Sci. Technol., 55, 16339–16346, https://doi.org/10.1021/acs.est.1c05901, 2021.

Liu, D., Allan, J., Whitehead, J., Young, D., Flynn, M., Coe, H., McFiggans, G., Fleming, Z. L., and Bandy, B.: Ambient black carbon particle hygroscopic properties controlled by mixing state and composition, Atmos. Chem. Phys., 13, 2015-2029, https://doi.org/10.5194/acp-13-2015-2013, 2013.

Liu, D., Whitehead, J., Alfarra, M. R., Reyes-Villegas, E., Spracklen, Dominick V., Reddington, Carly L., Kong, S., Williams, Paul I., Ting, Y.-C., Haslett, S., Taylor, Jonathan W., Flynn, Michael J., Morgan, William T., McFiggans, G., Coe, H., and Allan, James D.: Black-carbon absorption enhancement in the atmosphere determined by particle mixing state, Nat. Geosci., 10, 184-188, https://doi.org/10.1038/ngeo2901, 2017a.

Liu, D., Joshi, R., Wang, J., Yu, C., Allan, J. D., Coe, H., Flynn, M. J., Xie, C., Lee, J., Squires, F., Kotthaus, S., Grimmond, S., Ge, X., Sun, Y., and Fu, P.: Contrasting physical properties of black carbon in urban Beijing between winter and summer, Atmos. Chem. Phys., 19, 6749-6769, https://doi.org/10.5194/acp-19-6749-2019, 2019.

Liu, S., Aiken, A. C., Gorkowski, K., Dubey, M. K., Cappa, C. D., Williams, L. R., Herndon, S. C., Massoli, P., Fortner, E. C., Chhabra, P. S., Brooks, W. A., Onasch, T.

1069 B., Jayne, J. T., Worsnop, D. R., China, S., Sharma, N., Mazzoleni, C., Xu, L., Ng, N.

1070 L., Liu, D., Allan, J. D., Lee, J. D., Fleming, Z. L., Mohr, C., Zotter, P., Szidat, S., and

1071 Prevot, A. S. H.: Enhanced light absorption by mixed source black and brown carbon

1072 particles in UK winter, Nat. Commun., 6, 8435, https://doi.org/10.1038/ncomms9435,

1073 2015.

1074   Liu, Z., Lu, X., Feng, J., Fan, Q., Zhang, Y., and Yang, X.: Influence of Ship

1075 Emissions on Urban Air Quality: A Comprehensive Study Using Highly Time-Resolved

1076 Online Measurements and Numerical Simulation in Shanghai, Environ. Sci. Technol.,

1077 51, 202-211, https://doi.org/10.1021/acs.est.6b03834, 2017b.

1078   Ma, Y., Huang, C., Jabbour, H., Zheng, Z., Wang, Y., Jiang, Y., Zhu, W., Ge, X.,

1079 Collier, S., and Zheng, J.: Mixing state and light absorption enhancement of black

1080 carbon aerosols in summertime Nanjing, China, Atmos. Environ., 222, 117141,

1081 https://doi.org/https://doi.org/10.1016/j.atmosenv.2019.117141, 2020.

1082   Malmborg, V. B., Eriksson, A. C., Shen, M., Nilsson, P., Gallo, Y., Waldheim, B.,

1083 Martinsson, J., Andersson, O., and Pagels, J.: Evolution of In-Cylinder Diesel Engine

1084 Soot and Emission Characteristics Investigated with Online Aerosol Mass Spectrometry,

1085 Environ. Sci. Technol., 51, 1876-1885, https://doi.org/10.1021/acs.est.6b03391, 2017.

1086   Mar, V., Fulvio, A., Andrés, A., Xavier, Q., Teresa, M., Saúl García, D. S., María

1087 Dolores, H., and Rosalía, F. P.: Chemical tracers of particulate emissions from

1088 commercial shipping, Environ. Sci. Technol., 43, 7472-7477,

1089 https://doi.org/10.1021/es901558t, 2009.

1090   Massoli, P., Fortner, E. C., Canagaratna, M. R., Williams, L. R., Zhang, Q., Sun,

1091 Y., Schwab, J. J., Trimborn, A., Onasch, T. B., Demerjian, K. L., Kolb, C. E., Worsnop,

1092 D. R., and Jayne, J. T.: Pollution Gradients and Chemical Characterization

1093 of Particulate Matter from Vehicular Traffic near Major Roadways: Results from the

1094 2009 Queens College Air Quality Study in NYC, Aerosol Sci. Technol., 46, 1201-1218,

1095 https://doi.org/10.1080/02786826.2012.701784, 2012.

1096   Massoli, P., Onasch, T. B., Cappa, C. D., Nuamaan, I., Hakala, J., Hayden, K., Li,

1097 S.-M., Sueper, D. T., Bates, T. S., Quinn, P. K., Jayne, J. T., and Worsnop, D. R.:

1098 Characterization of black carbon-containing particles from soot particle aerosol mass

1099 spectrometer measurements on the R/VAtlantisduring CalNex 2010, J. Geophys. Res.:

1100 Atmos., 120, 2575-2593, https://doi.org/10.1002/2014jd022834, 2015.

1101 Mazzei, F., D'Alessandro, A., Lucarelli, F., Nava, S., Prati, P., Valli, G., and Vecchi,

1102 R.: Characterization of particulate matter sources in an urban environment, Sci. Total

1103 Environ., 401, 81-89, https://doi.org/10.1016/j.scitotenv.2008.03.008, 2008.

1104 Mohr, C., Huffman, J. A., Cubison, M. J., Aiken, A. C., Docherty, K. S., Kimmel,

1105 J. R., Ulbrich, I. M., Hannigan, M., and Jimenez, J. L.: Characterization of Primary

1106 Organic Aerosol Emissions from Meat Cooking, Trash Burning, and Motor Vehicles

1107 with High-Resolution Aerosol Mass Spectrometry and Comparison with Ambient and

1108 Chamber Observations, Environ. Sci. Technol., 43, 2443-2449,

1109 https://doi.org/10.1021/es8011518, 2009.

1110 Moldanová, J., Fridell, E., Popovicheva, O., Demirdjian, B., Tishkova, V.,

1111 Faccinetto, A., and Focsa, C.: Characterisation of particulate matter and gaseous

1112 emissions from a large ship diesel engine, Atmos. Environ., 43, 2632-2641,

1113 https://doi.org/10.1016/j.atmosenv.2009.02.008, 2009.

1114 Ng, N. L., Canagaratna, M. R., Jimenez, J. L., Chhabra, P. S., Seinfeld, J. H., and

1115 Worsnop, D. R.: Changes in organic aerosol composition with aging inferred from

1116 aerosol mass spectra, Atmos. Chem. Phys., 11, 6465-6474, https://doi.org/10.5194/acp-

1117 11-6465-2011, 2011.

1118 Onasch, T. B., Trimborn, A., Fortner, E. C., Jayne, J. T., Kok, G. L., Williams, L.

1119 R., Davidovits, P., and Worsnop, D. R.: Soot Particle Aerosol Mass Spectrometer:

1120 Development, Validation, and Initial Application, Aerosol Sci. Technol., 46, 804-817,

1121 https://doi.org/10.1080/02786826.2012.663948, 2012.

1122 Paatero, P., and Tapper, U.: Positive matrix factorization: A non-negative factor

1123 model with optimal utilization of error estimates of data values, Environmetrics, 5, 111-

1124 126, https://doi.org/10.1002/env.3170050203, 1994.

1125 Pathak, R. K., Wang, T., and Wu, W. S.: Nighttime enhancement of PM2.5 nitrate

1126 in ammonia-poor atmospheric conditions in Beijing and Shanghai: Plausible

1127 contributions of heterogeneous hydrolysis of N2O5 and HNO3 partitioning, Atmos.

1128 Environ., 45, 1183-1191, https://doi.org/10.1016/j.atmosenv.2010.09.003, 2011.

1129   Peng, J., Hu, M., Guo, S., Du, Z., Zheng, J., Shang, D., Levy, Z. M., Zeng, L.,
1130 Shao, M., and Wu, Y. S.: Markedly enhanced absorption and direct radiative forcing of
1131 black carbon under polluted urban environments, Proc. Natl. Acad. Sci. U. S. A., 113,
1132 4266-4271, https://doi.org/10.1073/pnas.1602310113, 2016.

1133   Petit, J. E., Favez, O., Albinet, A., and Canonaco, F.: A user-friendly tool for
1134 comprehensive evaluation of the geographical origins of atmospheric pollution: Wind
1135 and trajectory analyses, 88, 183-187, https://doi.org/10.1016/j.envsoft.2016.11.022,
1136 2017.

1137   Petters, M. D., and Kreidenweis, S. M.: A single parameter representation of
1138 hygroscopic growth and cloud condensation nucleus activity, Atmos. Chem. Phys., 7,
1139 1961-1971, https://doi.org/10.5194/acp-7-1961-2007, 2007.

1140   Ramanathan, V., and Carmichael, G.: Global and regional climate changes due to
1141 black carbon, Nat. Geosci., 1, 221-227, https://doi.org/10.1038/ngeo156, 2008.

1142   Rivellini, L.-H., Adam, M. G., Kasthuriarachchi, N., and Lee, A. K. Y.:
1143 Characterization of carbonaceous aerosols in Singapore: insight from black carbon
1144 fragments and trace metal ions detected by a soot particle aerosol mass spectrometer,
1145 Atmos. Chem. Phys., 20, 5977-5993, https://doi.org/10.5194/acp-20-5977-2020, 2020.

1146   Saarikoski, S., Timonen, H., Carbone, S., Kuuluvainen, H., Niemi, J. V., Kousa,
1147 A., Rönkkö, T., Worsnop, D., Hillamo, R., and Pirjola, L.: Investigating the chemical
1148 species in submicron particles emitted by city buses, Aerosol Sci. Technol., 51, 317-
1149 329, https://doi.org/10.1080/02786826.2016.1261992, 2016.

1150   Sun, Y. L., Zhang, Q., Schwab, J. J., Demerjian, K. L., Chen, W. N., Bae, M. S.,
1151 Hung, H. M., Hogrefe, O., Frank, B., Rattigan, O. V., and Lin, Y. C.: Characterization
1152 of the sources and processes of organic and inorganic aerosols in New York city with a
1153 high-resolution time-of-flight aerosol mass apectrometer, Atmos. Chem. Phys., 11,
1154 1581-1602, https://doi.org/10.5194/acp-11-1581-2011, 2011.

1155   Sun, Y. L., Zhang, Q., Schwab, J. J., Yang, T., Ng, N. L., and Demerjian, K. L.:
1156 Factor analysis of combined organic and inorganic aerosol mass spectra from high
1157 resolution aerosol mass spectrometer measurements, Atmos. Chem. Phys., 12, 8537-
1158 8551, https://doi.org/10.5194/acp-12-8537-2012, 2012.

1159   Topping, D. O., McFiggans, G. B., and Coe, H.: A curved multi-component aerosol

1160   hygroscopicity model framework: Part 2 – Including organic compounds, Atmos. Chem.

1161   Phys., 5, 1223-1242, https://doi.org/10.5194/acp-5-1223-2005, 2005a.

1162   Topping, D. O., McFiggans, G. B., and Coe, H.: A curved multi-component aerosol

1163   hygroscopicity model framework: Part 1 – Inorganic compounds, Atmos. Chem. Phys.,

1164   5, 1205-1222, https://doi.org/10.5194/acp-5-1205-2005, 2005b.

1165   Ulbrich, I. M., Canagaratna, M. R., Zhang, Q., Worsnop, D. R., and Jimenez, J. L.:

1166   Interpretation of organic components from Positive Matrix Factorization of aerosol

1167   mass   spectrometric   data,   Atmos.   Chem.   Phys.,   9,   2891-2918,

1168   https://doi.org/10.5194/acp-9-2891-2009, 2009.

1169   Ulbrich, I. M., Canagaratna, M. R., Cubison, M. J., Zhang, Q., Ng, N. L., Aiken,

1170   A. C., and Jimenez, J. L.: Three-dimensional factorization of size-resolved organic

1171   aerosol mass spectra from Mexico City, Atmos. Meas. Tech., 5, 195-224,

1172   https://doi.org/10.5194/amt-5-195-2012, 2012.

1173   Wang, J., Ge, X., Chen, Y., Shen, Y., Zhang, Q., Sun, Y., Xu, J., Ge, S., Yu, H., and

1174   Chen, M.: Highly time-resolved urban aerosol characteristics during springtime in

1175   Yangtze River Delta, China: insights from soot particle aerosol mass spectrometry,

1176   Atmos. Chem. Phys., 16, 9109-9127, https://doi.org/10.5194/acp-16-9109-2016, 2016.

1177   Wang, J., Zhang, Q., Chen, M., Collier, S., Zhou, S., Ge, X., Xu, J., Shi, J., Xie,

1178   C., Hu, J., Ge, S., Sun, Y., and Coe, H.: First Chemical Characterization of Refractory

1179   Black Carbon Aerosols and Associated Coatings over the Tibetan Plateau (4730 m a.s.l),

1180   Environ. Sci. Technol., 51, 14072-14082, https://doi.org/10.1021/acs.est.7b03973,

1181   2017.

1182   Wang, J., Liu, D., Ge, X., Wu, Y., Shen, F., Chen, M., Zhao, J., Xie, C., Wang, Q.,

1183   Xu, W., Zhang, J., Hu, J., Allan, J., Joshi, R., Fu, P., Coe, H., and Sun, Y.:

1184   Characterization of black carbon-containing fine particles in Beijing during wintertime,

1185   Atmos. Chem. Phys., 19, 447-458, https://doi.org/10.5194/acp-19-447-2019, 2019.

1186   Wang, J., Ye, J., Liu, D., Wu, Y., Zhao, J., Xu, W., Xie, C., Shen, F., Zhang, J.,

1187   Ohno, P. E., Qin, Y., Zhao, X., Martin, S. T., Lee, A. K. Y., Fu, P., Jacob, D. J., Zhang,

1188   Q., Sun, Y., Chen, M., and Ge, X.: Characterization of submicron organic particles in

Beijing during summertime: comparison between SP-AMS and HR-AMS, Atmos. Chem. Phys., 20, 14091-14102, https://doi.org/10.5194/acp-20-14091-2020, 2020a.

Wang, J., Ye, J., Zhang, Q., Zhao, J., Wu, Y., Li, J., Liu, D., Li, W., Zhang, Y., Wu, C., Xie, C., Qin, Y., Lei, Y., Huang, X., Guo, J., Liu, P., Fu, P., Li, Y., Lee, H. C., Choi, H., Zhang, J., Liao, H., Chen, M., Sun, Y., Ge, X., Martin, S. T., and Jacob, D. J.: Aqueous production of secondary organic aerosol from fossil-fuel emissions in winter Beijing haze, Proc. Natl. Acad. Sci. U. S. A., 118, e2022179118, https://doi.org/10.1073/pnas.2022179118, 2021.

Wang, S., Newland, M. J., Deng, W., Rickard, A. R., Hamilton, J. F., Muñoz, A., Ródenas, M., Vázquez, M. M., Wang, L., and Wang, X.: Aromatic Photo-oxidation, A New Source of Atmospheric Acidity, Environ. Sci. Technol., 54, 7798-7806, https://doi.org/10.1021/acs.est.0c00526, 2020b.

Willis, M. D., Healy, R. M., Riemer, N., West, M., Wang, J. M., Jeong, C.-H., Wenger, J. C., Evans, G. J., Abbatt, J. P. D., and Lee, A. K. Y.: Quantification of black carbon mixing state from traffic: implications for aerosol optical properties, Atmos. Chem. Phys., 16, 4693-4706, https://doi.org/10.5194/acp-16-4693-2016, 2016.

Wu, Y., Ge, X., Wang, J., Shen, Y., Ye, Z., Ge, S., Wu, Y., Yu, H., and Chen, M.: Responses of secondary aerosols to relative humidity and photochemical activities in an industrialized environment during late winter, Atmos. Environ., 193, 66-78, https://doi.org/10.1016/j.atmosenv.2018.09.008, 2018.

Wu, Y., Liu, D., Wang, J., Shen, F., Chen, Y., Cui, S., Ge, S., Wu, Y., Chen, M., and Ge, X.: Characterization of Size-Resolved Hygroscopicity of Black Carbon-Containing Particle in Urban Environment, Environ. Sci. Technol., 53, 14212-14221, https://doi.org/10.1021/acs.est.9b05546, 2019.

Wu, Y., Liu, D., Wang, X., Li, S., Zhang, J., Qiu, H., Ding, S., Hu, K., Li, W., Tian, P., Liu, Q., Zhao, D., Ma, E., Chen, M., Xu, H., Ouyang, B., Chen, Y., Kong, S., Ge, X., and Liu, H.: Ambient marine shipping emissions determined by vessel operation mode along the East China Sea, Sci. Total Environ., 769, 144713, https://doi.org/10.1016/j.scitotenv.2020.144713, 2021.

Wu, Z. J., Zheng, J., Shang, D. J., Du, Z. F., Wu, Y. S., Zeng, L. M., Wiedensohler,

1219 A., and Hu, M.: Particle hygroscopicity and its link to chemical composition in the

1220 urban atmosphere of Beijing, China, during summertime, Atmos. Chem. Phys., 16,

1221 1123-1138, https://doi.org/10.5194/acp-16-1123-2016, 2016.

1222 Xie, C., Xu, W., Wang, J., Liu, D., Ge, X., Zhang, Q., Wang, Q., Du, W., Zhao, J.,

1223 Zhou, W., Li, J., Fu, P., Wang, Z., Worsnop, D., and Sun, Y.: Light absorption

1224 enhancement of black carbon in urban Beijing in summer, Atmos. Environ., 213, 499-

1225 504, https://doi.org/10.1016/j.atmosenv.2019.06.041, 2019.

1226 Xu, J., Zhang, Q., Chen, M., Ge, X., Ren, J., and Qin, D.: Chemical composition,

1227 sources, and processes of urban aerosols during summertime in northwest China:

1228 insights from high-resolution aerosol mass spectrometry, Atmos. Chem. Phys., 14,

1229 12593-12611, https://doi.org/10.5194/acp-14-12593-2014, 2014.

1230 Xu, W., Han, T., Du, W., Wang, Q., Chen, C., Zhao, J., Zhang, Y., Li, J., Fu, P.,

1231 Wang, Z., Worsnop, D. R., and Sun, Y.: Effects of Aqueous-Phase and Photochemical

1232 Processing on Secondary Organic Aerosol Formation and Evolution in Beijing, China,

1233 Environ. Sci. Technol., 51, 762-770, https://doi.org/10.1021/acs.est.6b04498, 2017.

1234 Xu, W., Sun, Y., Wang, Q., Zhao, J., Wang, J., Ge, X., Xie, C., Zhou, W., Du, W.,

1235 Li, J., Fu, P., Wang, Z., Worsnop, D. R., and Coe, H.: Changes in Aerosol Chemistry

1236 From 2014 to 2016 in Winter in Beijing: Insights From High-Resolution Aerosol Mass

1237 Spectrometry, J. Geophys. Res.: Atmos., 124, 1132-1147,

1238 https://doi.org/10.1029/2018jd029245, 2019.

1239 Ye, Z., Liu, J., Gu, A., Feng, F., Liu, Y., Bi, C., Xu, J., Li, L., Chen, H., Chen, Y.,

1240 Dai, L., Zhou, Q., and Ge, X.: Chemical characterization of fine particulate matter in

1241 Changzhou, China, and source apportionment with offline aerosol mass spectrometry,

1242 Atmos. Chem. Phys., 17, 2573-2592, https://doi.org/10.5194/acp-17-2573-2017, 2017.

1243 Yu, G., Zhang, Y., Yang, F., He, B., Zhang, C., Zou, Z., Yang, X., Li, N., and Chen,

1244 J.: Dynamic Ni/V Ratio in the Ship-Emitted Particles Driven by Multiphase Fuel Oil

1245 Regulations in Coastal China, Environ. Sci. Technol., 55, 15031-15039,

1246 https://doi.org/10.1021/acs.est.1c02612, 2021.

1247 Yu, L., Smith, J., Laskin, A., Anastasio, C., Laskin, J., and Zhang, Q.: Chemical

1248 characterization of SOA formed from aqueous-phase reactions of phenols with the

triplet excited state of carbonyl and hydroxyl radical, Atmos. Chem. Phys., 14, 13801-13816, https://doi.org/10.5194/acp-14-13801-2014, 2014.

Zhang, F., Wang, Y., Peng, J., Chen, L., Sun, Y., Duan, L., Ge, X., Li, Y., Zhao, J., Liu, C., Zhang, X., Zhang, G., Pan, Y., Wang, Y., Zhang Annie, L., Ji, Y., Wang, G., Hu, M., Molina Mario, J., and Zhang, R.: An unexpected catalyst dominates formation and radiative forcing of regional haze, Proc. Natl. Acad. Sci. U. S. A., 117, 3960-3966, https://doi.org/10.1073/pnas.1919343117, 2020.

Zhang, G., Fu, Y., Peng, X., Sun, W., Shi, Z., Song, W., Hu, W., Chen, D., Lian, X., Li, L., Tang, M., Wang, X., and Bi, X.: Black Carbon Involved Photochemistry Enhances the Formation of Sulfate in the Ambient Atmosphere: Evidence From In Situ Individual Particle Investigation, J. Geophys. Res.: Atmos., 126, e2021JD035226, https://doi.org/10.1029/2021JD035226, 2021.

Zhang, Q., Canagaratna, M. R., Jayne, J. T., Worsnop, D. R., and Jimenez, J.-L.: Time- and size-resolved chemical composition of submicron particles in Pittsburgh: Implications for aerosol sources and processes, J. Geophys. Res., 110, https://doi.org/10.1029/2004JD004649, 2005.

Zhang, Q., Jimenez, J. L., Canagaratna, M. R., Ulbrich, I. M., Ng, N. L., Worsnop, D. R., and Sun, Y.: Understanding atmospheric organic aerosols via factor analysis of aerosol mass spectrometry: a review, Anal. Bioanal. Chem., 401, 3045-3067, https://doi.org/10.1007/s00216-011-5355-y, 2011.

Zhao, J., Qiu, Y., Zhou, W., Xu, W., Wang, J., Zhang, Y., Li, L., Xie, C., Wang, Q., Du, W., Worsnop, D. R., Canagaratna, M. R., Zhou, L., Ge, X., Fu, P., Li, J., Wang, Z., Donahue, N. M., and Sun, Y.: Organic Aerosol Processing During Winter Severe Haze Episodes in Beijing, J. Geophys. Res.: Atmos., 124, 10248-10263, https://doi.org/10.1029/2019jd030832, 2019.

Zhao, M., Zhang, Y., Ma, W., Fu, Q., Yang, X., Li, C., Zhou, B., Yu, Q., and Chen, L.: Characteristics and ship traffic source identification of air pollutants in China's largest port, Atmos. Environ., 64, 277-286, https://doi.org/10.1016/j.atmosenv.2012.10.007, 2013.

Zhou, S., Collier, S., Xu, J., Mei, F., Wang, J., Lee, Y.-N., Sedlacek, A. J.,

1279   Springston, S. R., Sun, Y., and Zhang, Q.: Influences of upwind emission sources and

1280   atmospheric processing on aerosol chemistry and properties at a rural location in the

1281   Northeastern   U.S,   J.   Geophys.   Res.:   Atmos.,   121,   6049-6065,

1282   https://doi.org/10.1002/2015jd024568, 2016.

1283
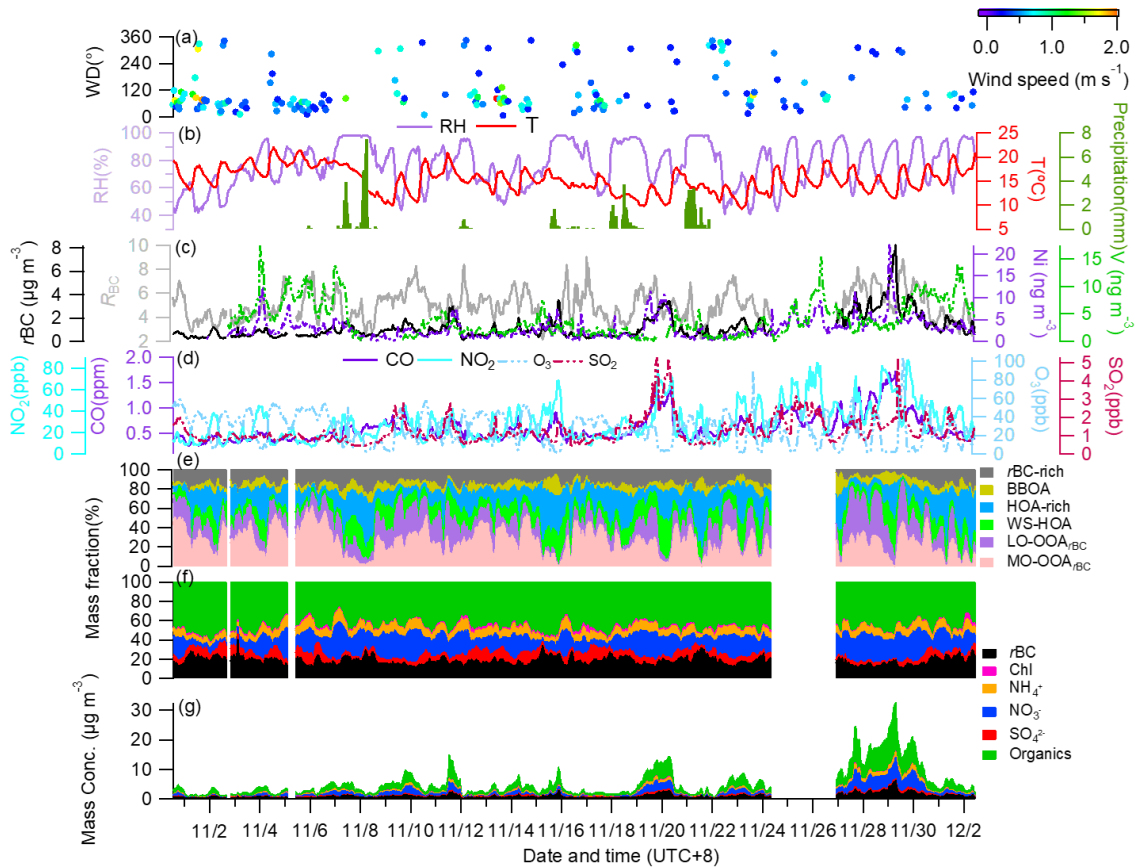
1284

1285 Figure 1. Time series of (a) wind direction (WD) colored by wind speed (WS), (b) air

1286 temperature (T), relative humidity (RH) and precipitation, (c) mass concentrations of

1287 rBC, Ni, V, and R_{BC} (mass ratio of all coating species to rBC), (d) mass concentrations

1288 of gas pollutants of CO, NO_2, O_3 and SO_2, (e) mass fractions (%) of different OA factors

1289 to the total rBCc OA, (f) mass fractions (%) of different components to the total rBCc

1290 mass, and (g) mass concentrations of stacked rBCc components.
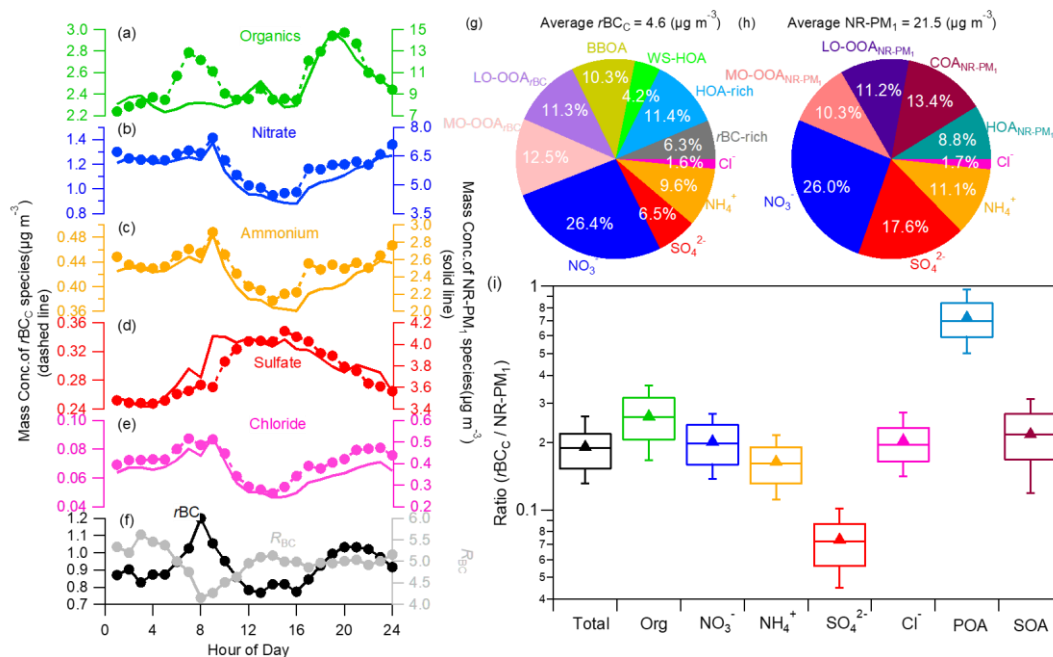
Figure 2. Diurnal cycles of mass concentrations of (a–e) rBCc and NR-PM$_1$ species (organics, nitrate, ammonium, sulfate, and chloride), and (f) rBC and R_{BC}. Campaign-average chemical composition of rBCc (g) and NR-PM$_1$ (h). (i) Mass ratios of species in rBCc to those in NR-PM$_1$ (the whiskers above and below the boxes mark the 90% and 10% percentiles, respectively; the upper and lower edge of the boxes represent the 75% and 25% percentiles, respectively; and the lines and triangles inside the boxes denote the median and mean values, respectively; SOA represents ([LO-OOA$_{r\mathrm{BC}}$] + [MO-OOA$_{r\mathrm{BC}}$])/([LO-OOA$_{\mathrm{NR-PM1}}$] + [LV-OOA$_{\mathrm{NR-PM1}}$]), and POA represents ([rBC-rich + HOA-rich + BBOA + WS-HOA])/HOA$_{\mathrm{NR-PM1}}$).
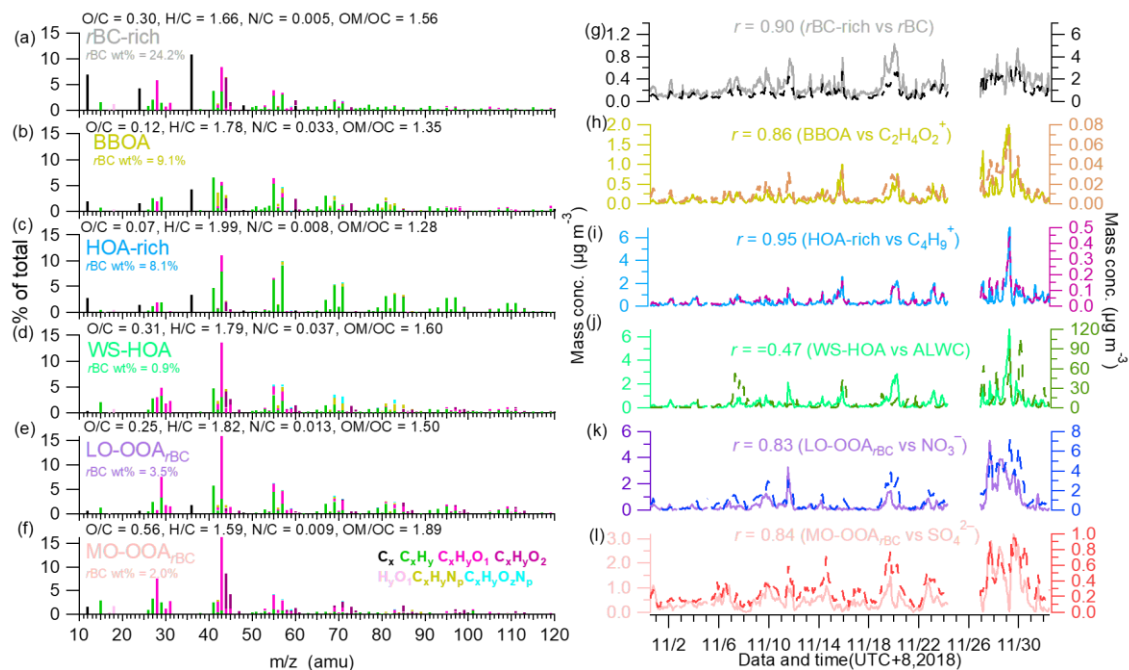
1301

1302 Figure 3. High resolution mass spectra of (a) *r*BC-rich, (b) BBOA, (c) HOA-rich, (d)

1303 WS-HOA, (e) LO-OOA*r*BC, and (f) MO-OOA*r*BC. (g-l) Time series of corresponding

1304 factors, their tracers (*r*BC, $C_2H_4O_2^+$, $C_4H_9^+$, ALWC, nitrate and sulfate) as well as the

1305 correlation coefficients (ALWC refers to aerosol liquid water content, which was

1306 estimated by using the model II of extended aerosol inorganic model (E-AIM II)(Clegg

1307 et al., 1998); calculation details and results at different RH values are described in the

1308 caption and shown in Fig. S5)

1309

1311
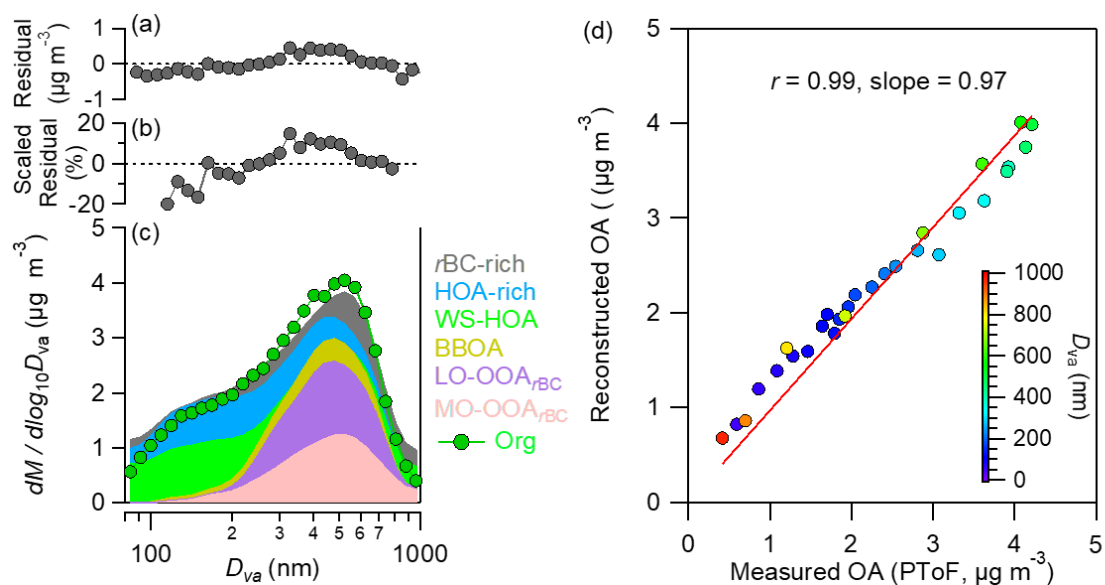
Figure 4. Summary of key diagnostic plots of derivation of size distributions of individual rBCc OA factors. (a) Absolute and (b) relative residuals between the reconstructed and measured OA mass concentrations in different size bins. (c) Stacked size distributions of the six OA factors compared to the size distributions of total OA. (d) Reconstructed OA mass concentrations compared to the measured values for different size bins (80-1000 nm).

1318
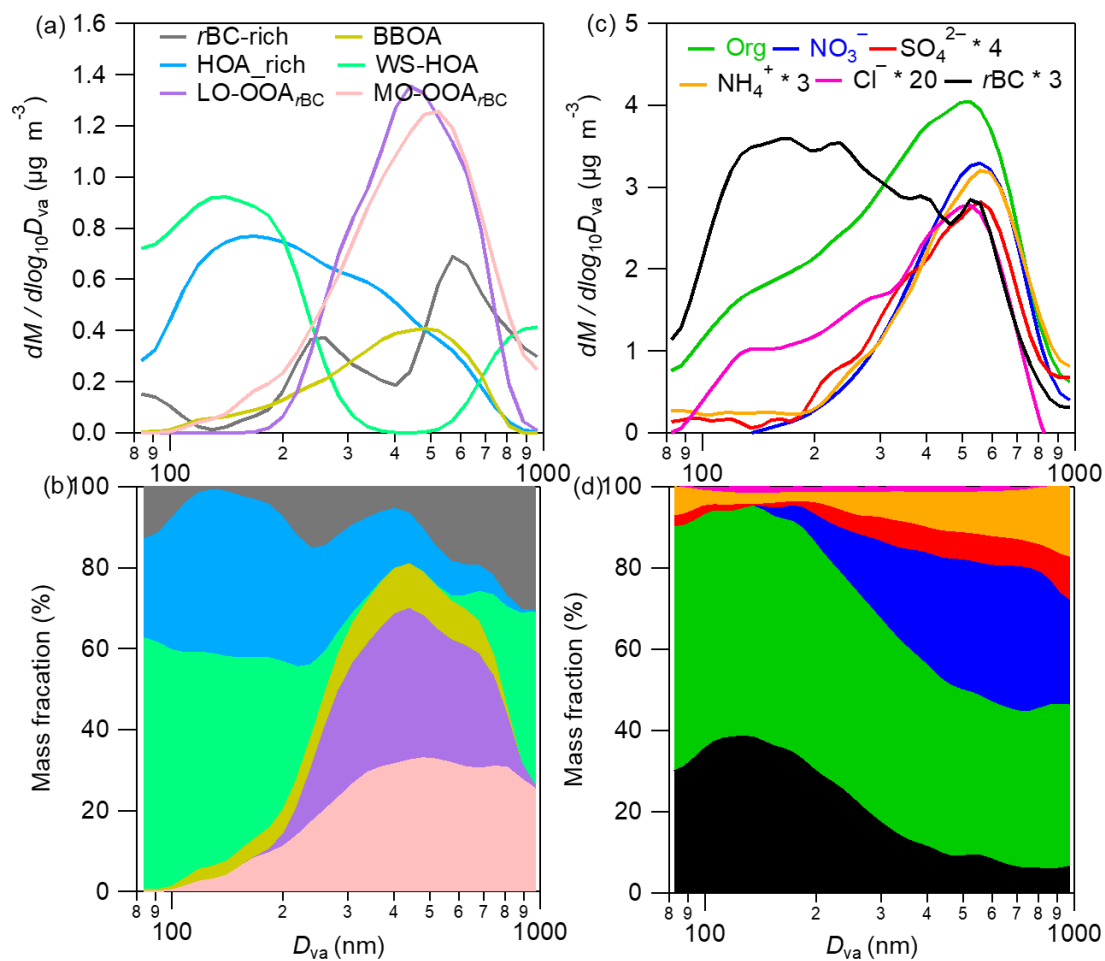
1319

1320 Figure 5. Campaign-average size distributions of six *r*BCc OA factors (a) and individual

1321 *r*BCc components (b), and corresponding mass contributions of the six factors to the

1322 total *r*BCc OA (c), and the major components to the total *r*BCc (d) at different sizes

1323 (80-1000 nm).

1324

1325
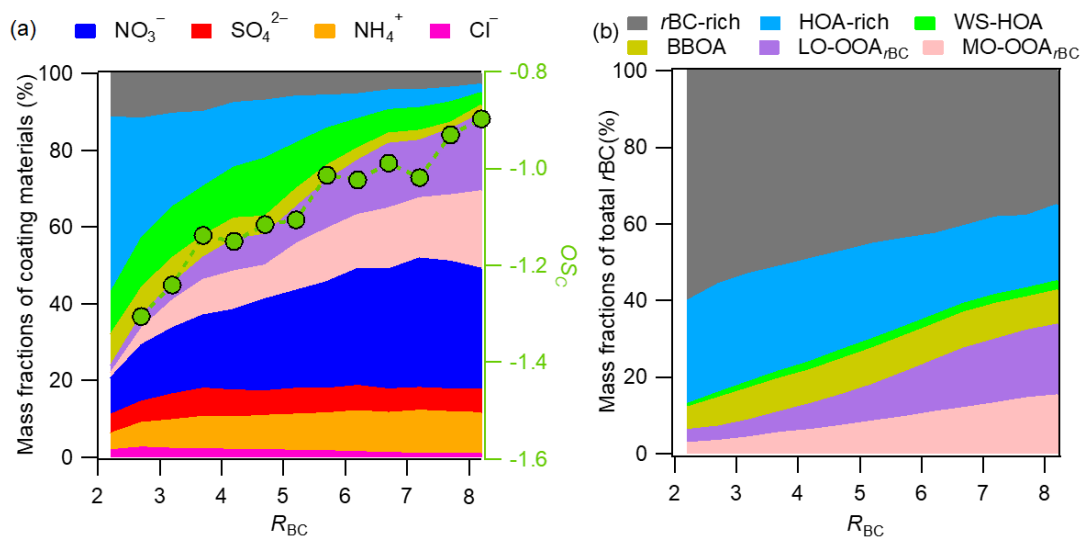
1326

1327 Figure 6. (a) Variations of mass fractions of the major *r*BCc components against R_{BC}.

1328 (b) Variations of mass contributions of individual *r*BCc OA factors to *r*BC against R_{BC}.

1329
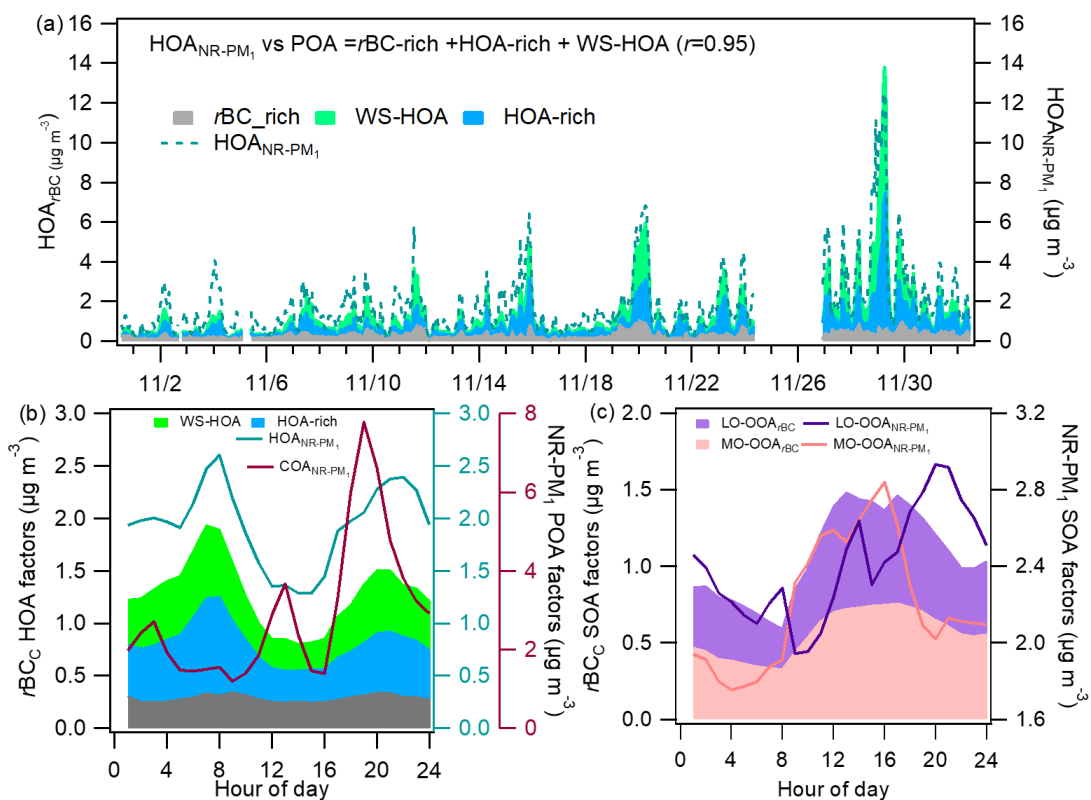
1330

1331   Figure 7. (a) Time series of stacked three rBCc POA factors (i.e., *r*BC-rich, HOA-rich,

1332   and WS-HOA) and HOA$_{NR-PM1}$. Comparisons of the diurnal patterns of different POA

1333   factors (b) and SOA factors (c) of *r*BCc and NR-PM$_1$.

1334
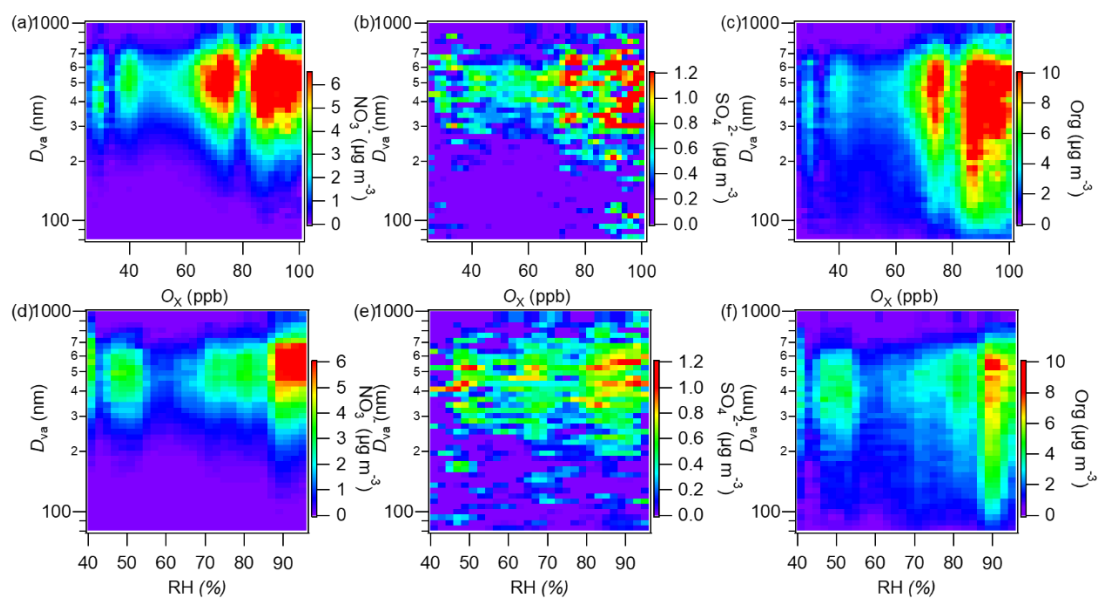
1337 Figure 8. Image plots of size distributions of *r*BCc nitrate, sulfate, organics as a function

1338 of (a-c) O_X and (d-f) RH, respectively (color represents its concentration).

1339
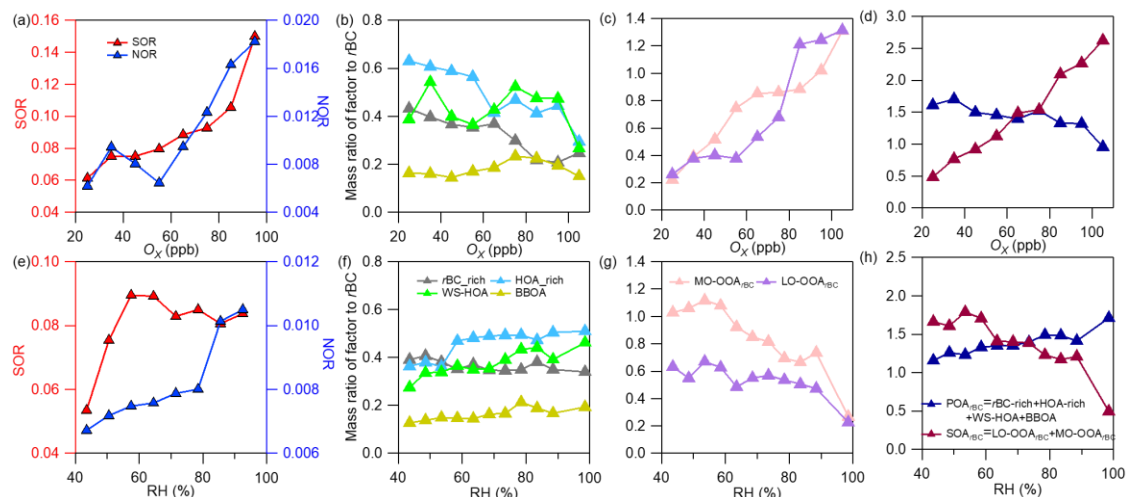
1340

1341 Figure 9. Variations of nitrogen oxidation ratio (NOR) and sulfur oxidation ratio, mass

1342 ratios of different POA factors, SOA factors and total POA and SOA to rBC against O_X

1343 (a-d) and RH (e-h) (NOR= $n\mathrm{NO}_3^-/(n\mathrm{NO}_3^-+n\mathrm{NO}_2+n\mathrm{NO})$ and SOR= $n\mathrm{SO}_4^{2-}/(n\mathrm{SO}_4^{2-}+n\mathrm{SO}_2)$,

1344 where $n\mathrm{NO}_3^-$, $n\mathrm{SO}_4^{2-}$, $n\mathrm{NO}_2$, $n\mathrm{NO}$ and $n\mathrm{SO}_2$ are the molar concentrations of particle-

1345 phase sulfate, nitrate, gaseous NO₂, NO and SO₂, respectively).

1346
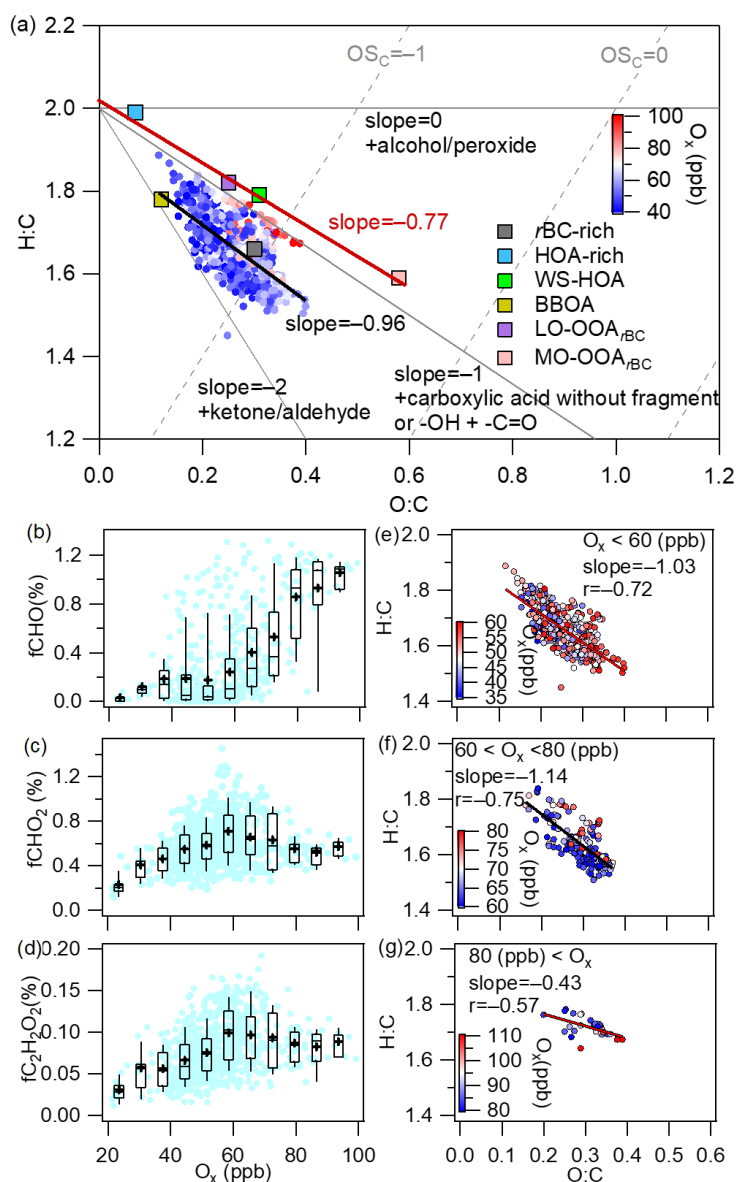
1347

Figure 10. (a) Van Krevelen diagram of H/C versus O/C ratios for all *r*BCc OA and the

six factors colored by O_X concentrations (the black line represents the linearly fitted

line of all OA data, and the red line is the fitted line of the four OA factors). (b-d) Mass

fractions of selected oxygenated ion fragments as a function of O_X (meanings of the

boxes are the same as those described in Fig. 2). (e-g) Scatter plots of H/C versus O/C

ratios under different O_X levels (data are colored by O_X concentrations).
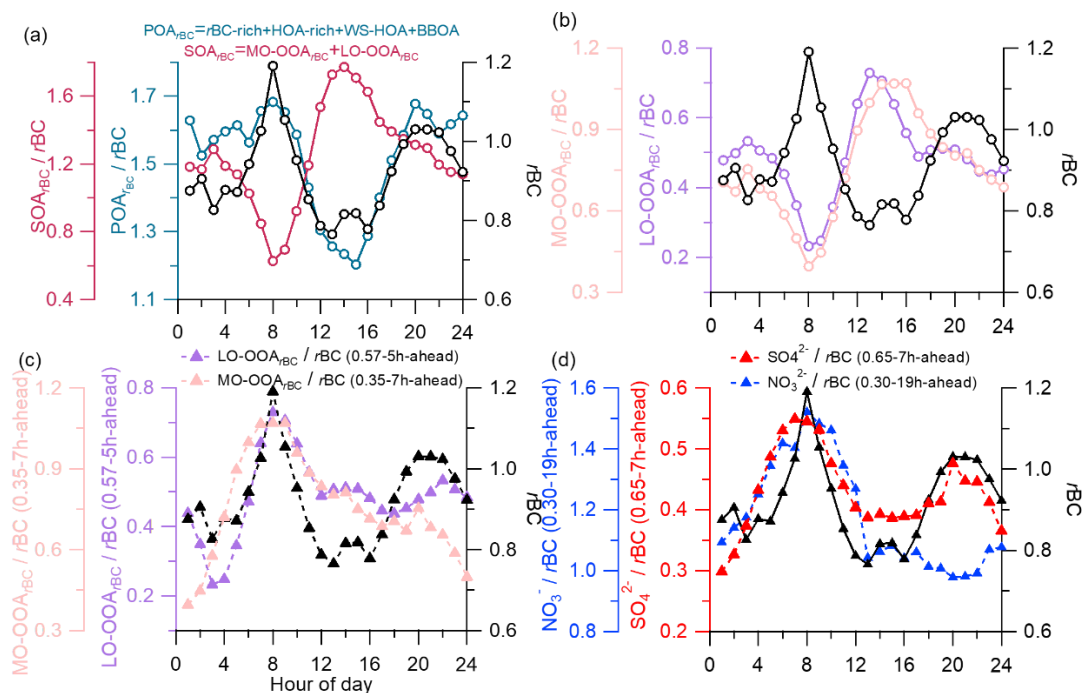
1354

Figure 11. Campaign-average diurnal patterns of (a) rBC, $POA_{r\text{BC}}/r$BC and $SOA_{r\text{BC}}/r$BC, and (b) rBC, $MO\text{-}OOA_{r\text{BC}}/r$BC and $LO\text{-}OOA_{r\text{BC}}/r$BC. Adjusted diurnal patterns by the average coating time (ACT) for (c) $LO\text{-}OOA_{r\text{BC}}/r$BC, $MO\text{-}OOA_{r\text{BC}}/r$BC, and (d) SO_4^{2-}/rBC, NO_3^{-}/rBC.

1359
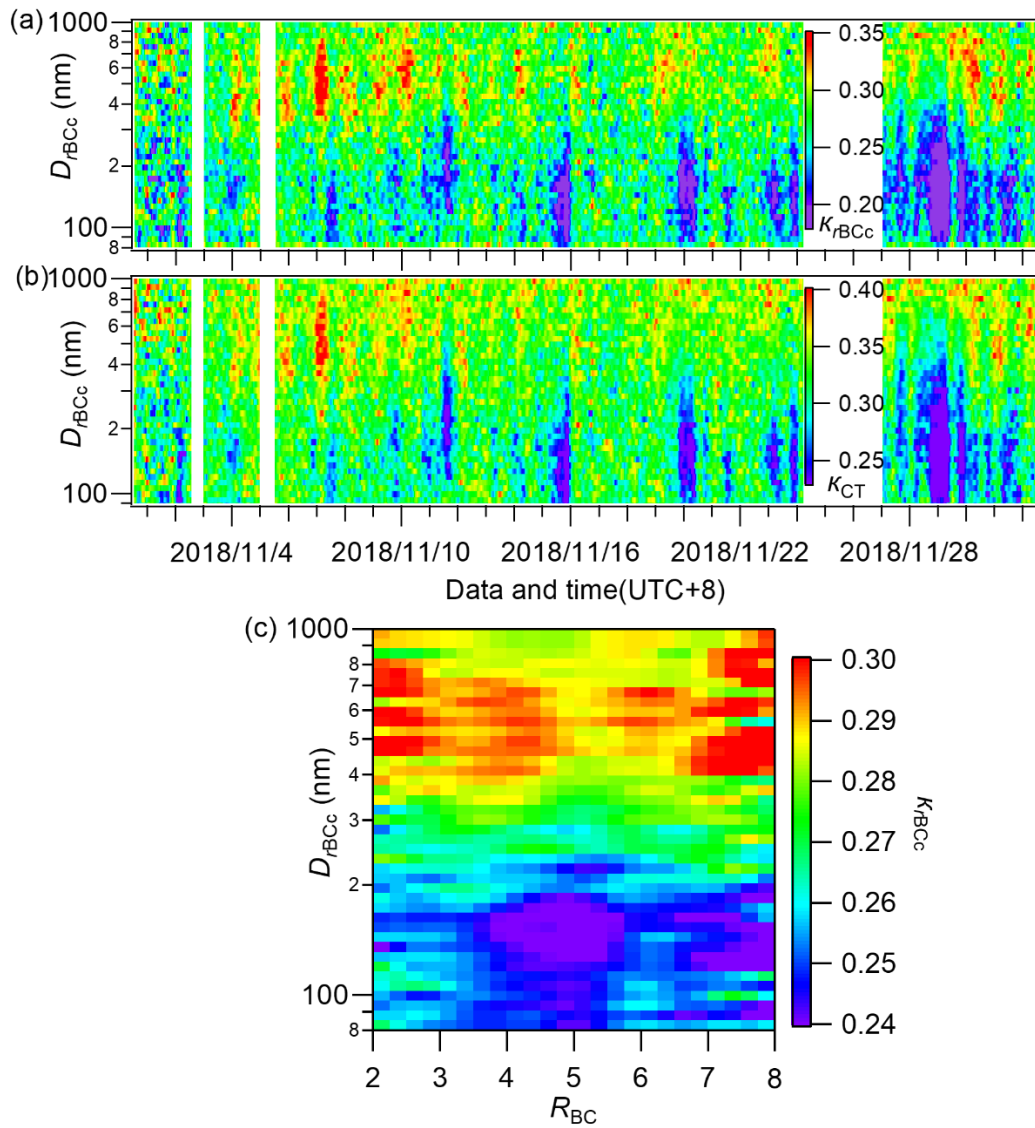
1360

1361 Figure 12. Image plots of size-resolved hygroscopicity parameters of (a) rBCc ($\kappa_{r\text{BCc}}$),

1362 (b) its coating materials (κ_{CT}) during the whole campaign, and (c) the campaign-average

1363 size-resolved $\kappa_{r\text{BCc}}$ at different R_{BC}.
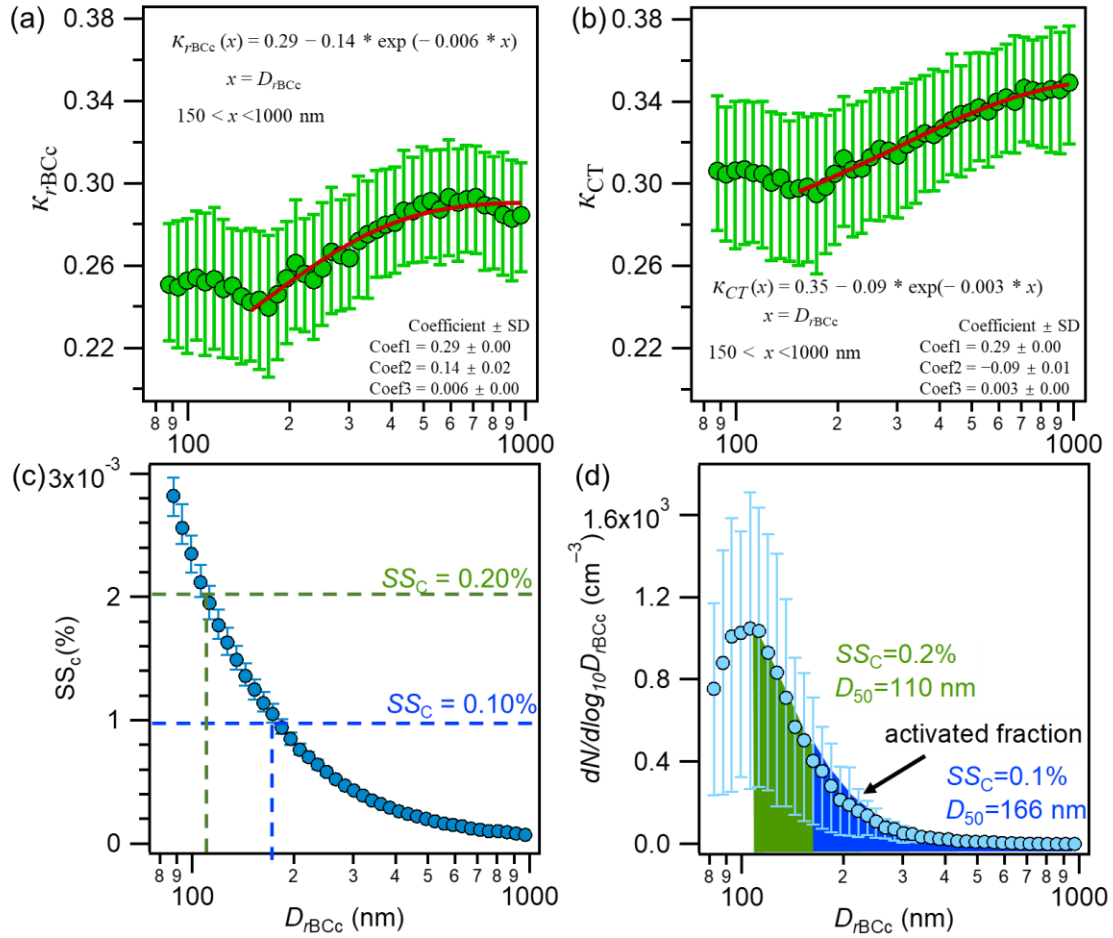
1364

1365   Figure 13. Campaign-average size-resolved hygroscopic parameters for rBCc ($\kappa_{r\text{BCc}}$)

1366   and (a) for its coatings (κ_{CT}) (b) (the red lines are exponential fits of the data of 150-

1367   1000 nm). (c) Campaign-average size-resolved critical supersaturation (SS_{C}), and (d)

1368   the predicted activated fraction of rBCc number concentration based on D_{50} at SS_{C} of

1369   0.1% (166 nm) and 0.2% (110 nm) (the solid circles are mean values, the upper and

1370   lower lines are the 75$^{\text{th}}$ and 25$^{\text{th}}$ percentiles, respectively).
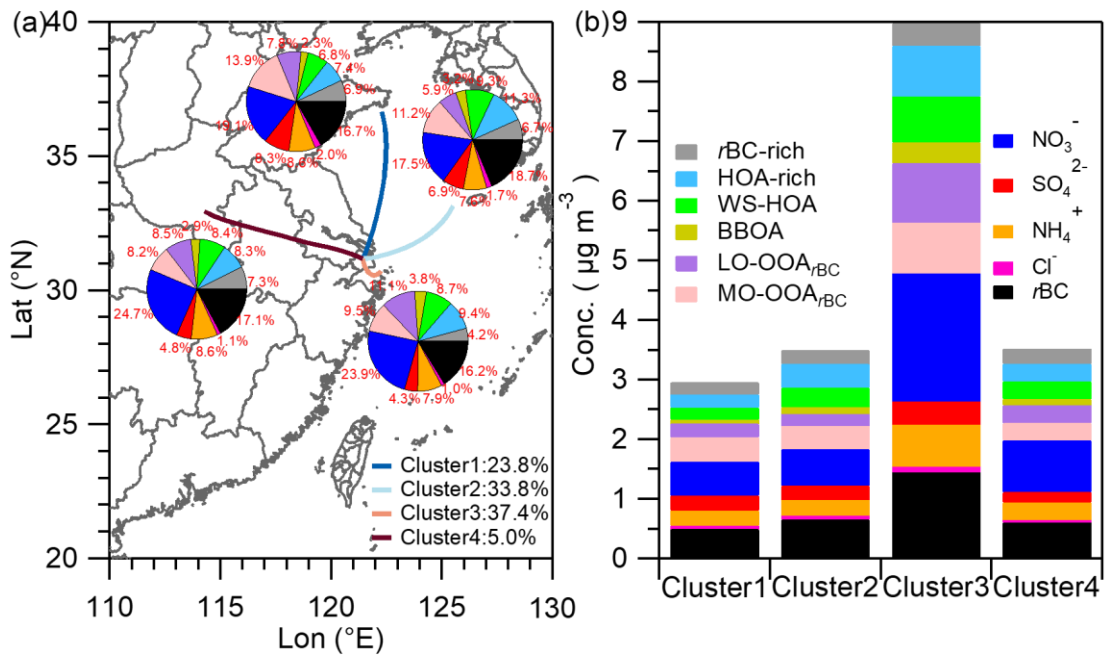
1371

1372   Figure 14. (a) Four clusters of 24-h backward trajectories (at altitude of 500 m) analyzed

1373   by NOAA HYSPLIT model (http://www.arl.noaa.gov/ready/hysplit4.html) embedded

1374   in Zefir(Petit et al., 2017), with the pie chart showing the average rBCc chemical

1375   compositions in each cluster. (b) Stacked mass concentrations of the rBCc components

1376   of the four clusters.
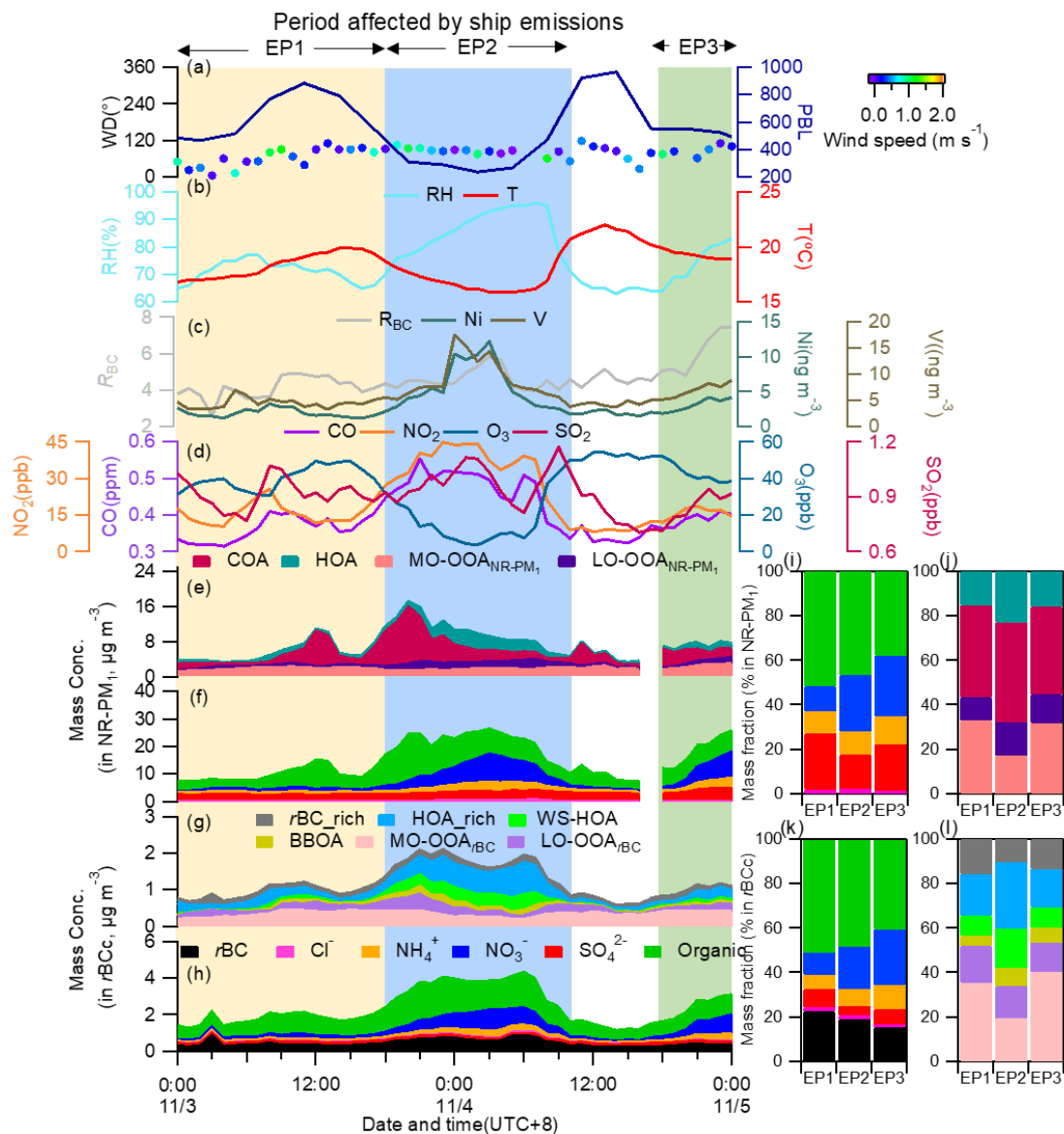
Figure 15. Time series of (a) wind direction (WD) colored by wind speed (WS), planetary boundary layer (PBL) height, (b) relative humidity (RH) and temperature (T), (c) mass concentrations of particle-phase Ni and V, and R_{BC}, (d) mass concentrations of CO, NO$_2$, O$_3$, SO$_2$, stacked concentrations of (e) NR-PM$_1$ OA factors, (f) NR-PM$_1$ species, (g) rBCc OA factors, and (h) rBCc components during the ship emission period (SEP). Mass contributions of different components to NR-PM$_1$ (i), different OA factors to total NR-PM$_1$ OA (j), different components to rBCc (k), and different OA factors to total rBCc OA (l) for the three episodes (EP1, EP2 and EP3).